Journal Pre-proof

Additively manufactured high-energy-absorption metamaterials with artificially engineered distribution of bio-inspired hierarchical microstructures

Zhenyang Gao, Hongze Wang, Hua Sun, Tengteng Sun, Yi Wu, Chu Lun Alex Leung, Haowei Wang

PII: S1359-8368(22)00718-1

DOI: https://doi.org/10.1016/j.compositesb.2022.110345

Reference: JCOMB 110345

To appear in: *Composites Part B*

Received Date: 3 May 2022

Revised Date: 8 September 2022

Accepted Date: 7 October 2022

Please cite this article as: Gao Z, Wang H, Sun H, Sun T, Wu Y, Alex Leung CL, Wang H, Additively manufactured high-energy-absorption metamaterials with artificially engineered distribution of bio-inspired hierarchical microstructures, *Composites Part B* (2022), doi: https://doi.org/10.1016/j.compositesb.2022.110345.

CRediT author statement

Zhenyang Gao: Conceptualization, Methodology, Software, Investigation, Data Curation, Validation, Formal analysis, Writing - Original Draft, Visualization, Writing - Review & Editing.

Hongze Wang: Conceptualization, Supervision, Resources, Funding acquisition, Project administration, Writing - Review & Editing

Hua Sun: Conceptualization.

Tengteng Sun: Data Curation.

Yi Wu: Supervision.

Chu Lun Alex Leung: Writing - Review & Editing

Haowei Wang: Supervision.

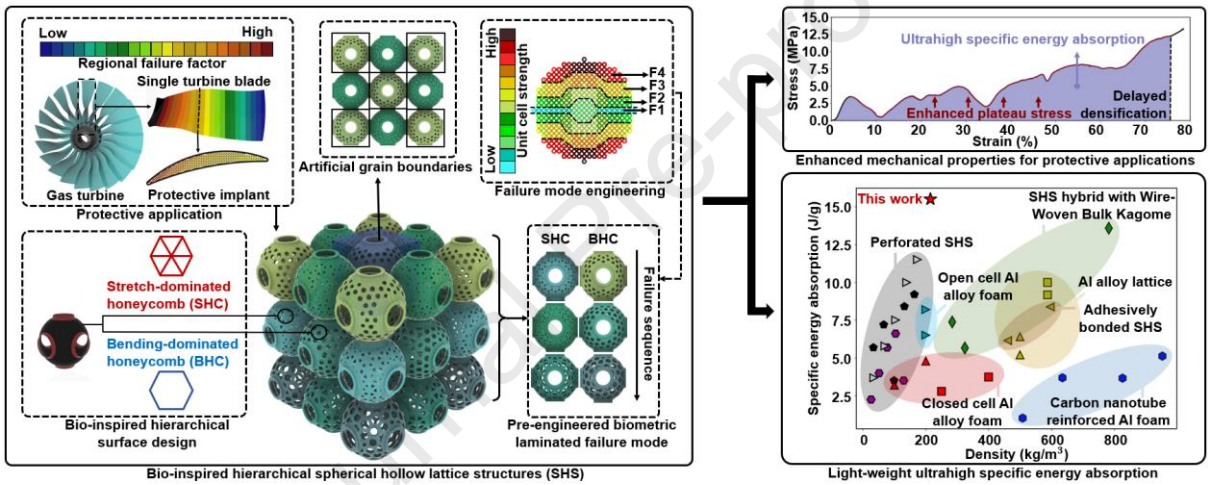

Additively manufactured high-energy-absorption metamaterials with artificially engineered distribution of bio-inspired hierarchical microstructures

Zhenyang Gao[a,b], Hongze Wang[a,b,c,d,e*], Hua Sun[a,b],Tengteng Sun[a,b], Yi Wu [a,b,c,*], Chu Lun Alex Leung[d,e] and Haowei Wang[a,b,c]

[a]*State Key Labortory of Metal Matrix Composites, Shanghai Jiao Tong University, Shanghai, 200240, China*

[b]*School of Materials Science and Engineering, Shanghai Jiao Tong University, Shanghai, 200240, China*

[c]*Institute of Alumics Materials, Shanghai Jiao Tong University (Anhui), Huaibei, 235000, China*

[d]*Department of Mechanical Engineering, University College London, London WC1E 7JE, UK*

[e]*Research Complex at Harwell, Harwell Campus, Oxfordshire OX11 0FA, UK*

[*]*This is to indicate the corresponding author, email: hz.wang@sjtu.edu.cn, eagle51@sjtu.edu.cn*

Abstract

There is an increasing demand of protective lightweight components in aerospace industries, and the high flexibility of additive manufacturing (AM) enables the design of complex structures to achieve such goal. In this study, a novel high-energy-absorption spherical hollow structure (SHS) was first engineered with a layer-wise failure mode and crystal-inspired grain boundaries through the variation of its hierarchical microstructures. To engineer the strength distribution of SHS, the mechanical properties of its spherical unit cells with bending-dominated and stretch-dominated honeycomb microstructures was experimentally studied with respect to different microstructural densities. Simulations were also performed to further reveal their failure mechanisms. Based on the relationship between the microstructural densities and the mechanical responses of these unit cells, a failure mode engineering method was proposed to artificially control the failure sequence of the lattice structure through a microstructural-controlled strength distribution. Here, we demonstrated a laminated failure mode composite hierarchical SHS lattice with crystal-inspired bending and stretch-dominated grains was developed using AM. Compared to different energy-absorption material designs with similar density, the quasi-static compressive results indicated that a hierarchical SHS lattice possesses a 72% improvement in the specific energy absorption, a 50% higher density-normalized plateau stress owing to the constraining effect of its mesoscale grain boundaries, and an increased number of intensively engineered laminated failure levels. This manuscript proposes a new design paradigm of AM high energy-absorption lattice structure for different protective applications.

Keywords: additive manufacturing, energy absorption, bio-inspired, metamaterials, failure mode engineering, composite structures

1. Introduction

Metamaterials are artificially engineered materials with complex microstructures designed to possess novel properties such as a high stiffness-to-weight ratio [1], a negative Poisson's ratio [2], improved fracture resistance [3, 4], improved damage tolerance [5, 6], vibration migration [7], multistability [8-11] and

enhanced specific energy absorption (SEA) [12], which have attracted huge interests from different research fields such as aerospace engineering [13] and biomedical science [14]. Additive manufacturing (AM) technology now allows researchers to develop materials with a precisely controlled microstructures without a significant increase in the manufacturing cost [15]. Numerous studies [16] have been conducted to evaluate the energy absorption and damage resistance advances of different metamaterials with innovative lattice structures. For instance, Wang et al. [17] proposed a modified body-centered-cubic (MBCC) lattice structures with biometric features inspired by the deep-sea glass sponge, where numerical and experimental studies indicates that the MBCC lattice structure exhibits a larger specific energy absorption (SEA) than its conventional counterpart. Based on the homogenization-based topology optimization method, Zhang et al. [18] improved the structural efficiencies of the pyramidal lattice structures with structural hierarchies, where an improved energy absorption capacity is observed. A spherical body-centered-cubic-shell composite lattice structure [19] made of additive manufactured (AM) carbon nanotube reinforced polyimide, which provides a higher energy absorption value and a larger energy absorption scale factor with different lattice densities compared to traditional elastomer foams. Sajadi et al. [20] 3D-printed spherical architected structures with silica-filled preceramic polymers and coated the surface of the spherical lattice with a flexible epoxy polymer. The proposed surface modification technique has proved to be effective in improving the damage tolerance of ceramic-based composite lattices compared to their counterparts. Among the different metamaterial structural designs, the spherical hollow structure (SHS) [21, 22] exhibits tremendous energy absorption and is lightweight because of the high porosity and highly plastic behavior of its microstructure. To explore the relationship between the energy absorption behavior and the design parameters of SHS materials, their mechanical properties were widely investigated as a function of sphere sizes [23], packing patterns [24], and relative densities [25]. Nevertheless, the SHS structures proposed in [23-25] were manufactured with identical hollow spheres and their structure was not optimized to further unlock its true energy absorption potential. With an increasing demand of the protective and damage-resistance lightweight materials in nowadays aerospace industries, the development of lattice metamaterial with a more significant improvement of their protective energy absorption performance is desired [26]. Although several innovative composite design features including the hybrid wire-woven bulk kagome [27], tailored distributions of the cell sizes [28], density-graded shells [29] have been recently proposed to enhance the energy absorption and impact performance of SHS structures, the design complexity offered by AM is still not fully explored to generate SHS lattices with more complicated structural features that could further assist the energy absorption, such as the multiscale hierarchies.

To achieve a further improvement in energy absorption, innovative design method of metamaterials is required to make simultaneous improvement in different mechanical aspects including the plateau stress, plateau duration, and the strength-normalized plateau magnitude. We propose a new design paradigm to tailor microstructures of the lattice with more optimized distribution of mechanical properties. Similar design approach has been considered by other research groups to achieve novel mechanical properties including the damage tolerance [5], permeability control [30], crack path control [3], advanced material characterization [31] and fracture resistance [32]. Nevertheless, the existing energy-absorbing protective metamaterial design usually possesses a uniformly distributed microstructures, or with simple structural variations, which usually fails in contemporarily accomplishing these mechanical advancements. Moreover, limited research approaches have been devoted to the improvement of energy absorption capability for the

lattice structure by artificially engineering its microstructure distributions. Therefore, it is desired to explore a general and effective design strategy to distribute the microstructure of the lattice for a higher energy absorption value.

Most biological structures have evolved with interesting patterns of hierarchical microstructures to achieve excellent mechanical performance. These features effectively increase survivability in severe natural environments and thus act as a valuable design database for material scientists to develop materials with advanced properties such as the crack deflection [4] or the fracture toughening [33]. Gu et al. [34] proposed a crack-arresting material mimicking the he hierarchical structures of the conch-shell which consists of alternating sheets of mineralized calcium carbonate structures separated by organic layers. Their results revealed that the catastrophic failure mode of the structure can be prevented by increasing the number of hierarchical levels. Meza et al. [35] studied the mechanical robustness and damage tolerance of hierarchically designed nano-lattices with three orders of octahedron hierarchical structures, wherein the combinations of solid polymers, hollow ceramics, and polymer/ceramic composites were compared. It was found that an appropriate hierarchical design of the microstructures can efficiently distribute the load over each region of the entire structure. Designing the lattice structures with bio-inspired hierarchies, *e.g.* artificially alternated hierarchical microstructures, is a promising approach for the development of next-generation energy-absorption protective lattice structures.

In this work, the SHS lattice structures were tailored with artificially distributed biomimetic hierarchical microstructures, and a significant improvement in the SEA was observed for the composite SHS lattice structures with the pre-engineered biometric laminated failure mode and crystal-inspired mesoscale grain boundaries. The structure of honeycomb is selected as the hierarchical microstructure exhibits excellent mechanical energy absorption performance [36]. To achieve distinct mechanical properties of different artificial grains for the lattice structure, two types of hierarchical honeycomb-inspired topology were applied: (1) a stretch-dominated honeycomb (SHC) and (2) a bending-dominated honeycomb (BHC). In Section 2, discussions are provided for the design and fabrication of single BHC and SHC hierarchical SHS unit cells with different microstructural densities. Based on the simulation and experimental results in Section 3, the relationship between the microstructural density and mechanical properties of biometric hierarchical SHS unit cells is established, and a failure mode engineering strategy of hierarchical SHS lattice structures is proposed. In addition, Section 3 details the experiments that were performed to study the effects of the gradient magnitude for hierarchical SHS lattice structures with a pre-engineered layer-wise failure sequence, wherein two types of hierarchical topologies with optimal gradient levels were combined to form a composite SHS lattice structure with artificially engineered grain boundaries. The failure mechanisms of the proposed lattice structures were characterized on the basis of the experimental deformation results, while the normalized average plateau stress, densification strain, SEA, and specific strength were derived and analyzed on the basis of the stress-strain curves. At the end of the paper, the conclusions are presented, and future research potentials are pointed out.

2. Method

In this section, the design and modeling strategy is provided to generate hierarchical SHS unit cells, where the SLM technique is applied to fabricate the unit cell samples. Section 2.1 details the design method for the hierarchical SHS unit cells. The hierarchical SHS unit cells with SHC and BHC microstructures are

fabricated with a range of microstructural densities, see Section 2.2. Exploring the mechanical behaviors of these fabricated unit cells with respect to their microstructural densities allows the failure mode engineering of a complicated hierarchical SHS lattice structure.

2.1. Design of hierarchical SHS unit cell

The structure of honeycomb is proven to exhibit advanced energy absorption capability according to previous studies [36-38], which is selected as the topology of the unit cells in this paper. To form effective artificial grain boundaries within the hierarchical SHS lattice structures, the mechanical properties of the unit cells between adjacent grains are required to be distinct [5]. Therefore, we developed the hierarchical structures of the unit cells with either stretch-dominated or bending-dominated mechanical features. The procedure for designing a hierarchical SHS unit cell can be generally divided into three processes: (1) the generation of the surface of a pure SHS unit cell; (2) the development of a biomimetic microstructural cutting wireframe; and (3) the Boolean operation between the surface of the pure SHS unit cell and hierarchical cutting wireframe. The detailed design flow is shown in Figure 1. In this study, the honeycomb structure was applied as the hierarchical design of the surface microstructures for SHS unit cells owing to its enhanced mechanical energy absorption properties, wherein a BHC and a SHC microstructural designs were created based on the Maxwell's stability criterion [39] on the 2D surface as shown in Figure 2 so that different compressive failure mechanisms could be achieved. The Maxwell's stability criterion is given in Equation (1) [39]:

$$M = b - 2j + 3 \tag{1}$$

where M is a factor to reflect the dominated deformation mechanisms of 2D lattice structures, b is the number of beams, and j is the number of nodes. It should be noted that the 2D Maxwell's stability criteria is applied, which is due to the fact that the designed hierarchical features are restricted within the surfaces of the SHS lattice structures rather than the 3D design space. For $M \geq 0$, the structure of the lattice tends to be stiffer with a stretch-dominated deformation mechanism otherwise, the lattice is more likely to be complaint with a bending-dominated deformation. In this study, the bending-dominated honeycomb microstructure is designed with $M = -3$, while a $M = 0$ is achieved for the stretch-dominated honeycomb microstructure. The surface of a pure SHS unit cell is developed on the basis of the Boolean assembly of the bonding surfaces and base sphere wherein the size of the bonding surface l and radius of the base sphere R are required. To design the geometry of the bonding surface as shown in Figure 3, the related design parameters are restricted based on Equations (2) and (3) to reduce the stress concentrations between adjacent SHS unit cells:

$$(R + r)/R = R/(R - l) \tag{2}$$

$$k_{P_i} = f''(x_{P_i})/[(1 + (f'(x_{P_i}))^2)^{\frac{3}{2}}] = 0 \tag{3}$$

where r is the radius of the circle O_3 tangent to the cross-sectional curve of the bonding surface, P_i represents the tangential points between the bonding surface and the base sphere, $f(x)$ describes the cross-sectional curve of the bonding surface, and k_{P_i} calculates the curvature of $f(x)$ at P_i.

To develop the hierarchical cutting wireframe, three subprocesses were performed: (1) the generation of the spherical bio-inspired polyhedron, (2) the separation of the base sphere, and (3) the extraction, offset, and fillet operation of the borders for individual topological surfaces. An open-source plug-in named Polyhedron is utilized in Rhino 6 [40] to obtain the bending-dominated honeycomb and stretch-dominated

honeycomb polyhedron; the edges of these polyhedrons are offset and sphericalized to the base sphere, as shown in Figure 1. The microstructural density of a polyhedron ρ_m was represented by the total number of the topological faces per unit cell. To derive the cutting geometry, the base sphere is divided into individual topological surfaces based on the spherical polyhedral wireframe. Subsequently, the border of each individual topological surface is extracted and offset toward its geometrical center with half of beam thickness d, wherein the offset wireframe is also tailored with filleted corners to decrease the stress concentrations within the structures of the hierarchical SHS unit cells.

Once the surface of the pure SHS unit cell and the geometry of the microstructural cutting wireframe were generated, Boolean operations could be performed to form the hierarchical SHS unit cells. The surface of the hierarchical SHS unit cell was created by removing the microstructural patterns that were separated by the cutting wireframe, and the solidified hierarchical SHS unit cells were developed by offsetting this surface with shell thickness t.

2.2. Fabrication of hierarchical SHS unit cells

In this study, the failure mode engineering method of the composite SHS lattice structure is achieved based on engineering the distribution of its unit cells with controlled mechanical properties, where compressive behaviors of these unit cells are explored to model the relationships between their microstructural design parameters and mechanical properties. There are two reasons of using the single unit cells for this mechanical modelling: (1) the macroscale failure sequence of the SHS lattice structure is engineered based on the control of the mechanical properties for its hierarchical unit cells, so the study of single unit cells is preferred; (2) using the single unit cells could result in a more precise modelling of their mechanical properties, since the obtained resulted will not be affected by the macroscale failure sequences of the tessellated arrangements. Therefore, the hierarchical SHS unit cells with BHC and SHC microstructures and 20-cm-sized in xyz directions were designed at different microstructural densities and fabricated through SLM technology as shown in Figure 4. For each type of the hierarchical microstructure, five microstructural densities were developed. Table 1 summarizes the design parameters of the hierarchical SHS unit cells, wherein the beam thickness, the shell thickness, and the lower limits of the microstructural densities were determined on the basis of the balance achieved by offering the smallest relative density while maintaining a good geometrical agreement between the CAD design and fabrication results of the hierarchical SHS unit cells. The AlMgScZr powder, as shown in Figure 5(a), was selected as the building material. Specifically, the powder of the build material is composed of 93.6% Al, 4.7% Mg, 0.79% Sc, 0.32% Zr, and 0.59% Mn. The detailed scanning electron microscope (SEM) images of the elementary distributions of the powder are shown in Figure S1. The powder is elemental mixed, and preserved in the 75° dryer for 12 hours before use. The EOS M280 SLM printer is selected as the build platform, where the sample in this study is fabricated based on a moving laser that selectively melts the designed region layer by layer based on the slicing data of the .stl files. To fabricate the samples, a 370 W laser with 1600 mm/s scanning speed is applied with 30 μm layer thickness, where the detailed information on the building setup and the process parameters are listed in Table 2. Since the powder is the patented Scalmalloy® provided by the Airbus [41], these processing parameters are selected based on the technical advice from the powder provider and preliminary experiments that produces a balanced mechanical performances and geometrical accuracies for complex structures. The mechanical properties of the as-built AlMgScZr alloys were

obtained through tensile tests based on the ASTM E8 standard, and revealed that the as-built AlMgScZr alloy possessed an average modulus of 75 GPa, yield stress of 366 MPa, ultimate stress of 422 MPa, and fracture strain of 19% as shown in Figure 5(b). The standard deviations of the mechanical properties of the specimens are 5.2 GPa, 12.7 MPa, 13.2 MPa, and 1.5% for modulus, yield stress, ultimate stress, and fracture strain, respectively. This result indicates a good consistency of the mechanical performance among the printed samples.

To improve the accuracy of the simulation, the structural dimensions of the as-built hierarchical SHS unit cells were measured using an optical microscope and compared with the original designs. For each hierarchical SHS unit cell, measurements were performed for a representative unit area with a full range of beam angles, as shown in Figure S2(a), with the measurement results summarized in Figure S2(b). The optical measurement captures are further provided in Figure S3 and Figure S4, where finer observations of the surface finish and the beam thicknesses are conducted. The beam thickness of the hierarchical SHS unit cells ranged from 887 μm to 1055 μm, which offset -113 μm to $+55$ μm from the designed value, while the shell thicknesses of hierarchical SHS unit cells was offset approximately -100 μm to -200 μm from the original designs. As reported in previous studies [42-44], numerous factors related to the SLM process can potentially cause geometrical variations, such as partially melted metal particles and large overhanging angles. These flaws were typically related to the nature of the SLM process and led to a reduction in the geometrical accuracy and mechanical properties of the built materials. Thus, the simulation models of the hierarchical SHS unit cells were corrected based on the experimental observations of the beam and shell thickness to provide a more accurate prediction of the stress distribution of the hierarchical SHS unit cells during the compression tests.

3. Results and discussions

To distribute the unit cells of a hierarchical SHS lattice with different microstructural types and densities to achieve an artificial failure mode design, theoretical models were established based on experimental and simulation efforts in Section 3.1, and focus on the microstructural density, relative density, density, compressive strength, and energy absorption capacity for hierarchical SHS unit cells with BHC and SHC microstructures. Based on these theoretical models, the failure mode engineering method was derived in Section 2.2, which details a biomimetic composite hierarchical SHS lattice structure with a layer-wise failure mode and artificially engineered grain boundaries in Section 3.3. This unique lattice structure resulted in a SEA of 15.25 J/g, densification strain of 0.75, and strength-normalized average plateau stress number of 2.

3.1. Mechanical modeling of hierarchical SHS unit cells

To study the compressive characteristics of the hierarchical SHS unit cells and to model their mechanical properties based on the topological types and densities, compressive experiments and simulations. The detailed recordings of the simulations are given in Video S1 and Video S2. During the compressive process, the compression rate was set to 2 mm/min to satisfy the quasi-static condition of the compression, wherein each unit cell was compressed beyond its densification stage. The Abaqus explicit model with VUMAT elemental failure analysis method is applied to perform finite element studies in this work, while the detailed configurations of the simulations are provided in Figure S5. Specifically, the unit cell surface models are

generated in Rhino 6, and are imported as shell objects to Abaqus with the thickness values summarized in Figure S2. A pair of rigid-body plates are used as the compressive objects, while a uniform compressive displacement and a fixed boundary is assigned to the upper and lower plate, respectively. The Abaqus S4R mesh elements are applied to perform the mechanical simulations for complicated surface geometries with hierarchical structures. Figure 6(a-b) provides the experimental stress-strain curves of the BHC and SHC hierarchical SHS unit cells with different microstructural densities. Compared with the experimental results, a postponed fracture is observed in the simulations, as shown in Figure 6(c-d). Such delayed failures are also reflected in the simulational stress-strain curves in Figure S5. In addition, the simulational stress-strain curves exhibit higher magnitude of stresses than those for experiments. This is due to the intrinsic SLM defects of the as-built hierarchical SHS unit cells, such as pores, voids, and powder adhesion [45, 46], which also resulted in the observation of a rough surface finish, as shown in Figure S3 and Figure S4. These defects caused a higher stress concentration and, hence, an earlier plastic deformation of the structures and reduced mechanical performance. Combining the experimental stress-strain curves with the simulated failure sequence and the stress distribution results, the compressive process of the hierarchical SHS unit cells with BHC microstructures could be characterized into four stages:

- I: The first wavy stage, wherein one of the top/bottom areas (A) collapsed.
- II: The secondary wavy stage, which corresponded to the collapse of the top/bottom area (A) that persisted in stage I, and the post-collapse deformation of the regions that were deformed at stage I.
- III: The plateau stage, wherein plastic deformation occurred in the middle area (B).
- IV: The densification stage, wherein the entire structure of the unit cells was forced to contract.

For the unit cells with SHC microstructures, different characterization of the failure sequence was observed:

- I-II: The wavy stage, wherein the middle area (B) collapsed.
- III: The plateau stage, which corresponded to the continuous collapse and fracture of the middle area (B).
- IV: The densification stage, wherein both the top and bottom areas (A) failed, and the entire structure of the unit cells was forced to contract.

Owing to the distinct failure sequences caused by the microstructural designs, large variations in strain limits and the relative stress magnitudes of each compressive stage were observed between the hierarchical SHS unit cells with BHC and SHC microstructures. Typically, the stretch-dominated structures will lead to a larger compressive strength and decreased stress plateau, while opposite phenomenon are usually observed for bending-dominated structures [47]. The unit cells with BHC microstructures showed bending-dominated behavior with a higher strength-normalized plateau stress and a longer plateau stage, while the unit cells with SHC microstructures exhibit a stretch-dominated behavior with 31%-74% larger compressive strength but limited plastic deformation. To explain, the plateau stage of the unit cells with BHC microstructures accounted for approximately 70% of the total strain, which was twice the value for those with SHC microstructures (35%). The upper range of the wavy strain for the unit cells with SHC microstructures was approximately 55%-60%, which was significantly broader than the approximately 30%-35% for the unit cells with BHC microstructures. The differences of the mechanical behaviors for BHC and SHC unit cells are provided in **Error! Reference source not found.** and summarized in four aspects: (1) the failure sequences of the unit cells are different. The SHC unit cells has a B1-B2-A failure mode where the initial collapse occurs at the middle regions, while the BHC unit cells possess an A1-A2-

B failure mode where the structures fail initially at the sides. (2) The resulted stress-strain curves of the unit cells are different. The BHC unit cells have a higher magnitude and doubled duration of the plateau than SHC unit cells, while SHC unit cells exhibit larger compressive strengths. These observations confirm the design intuitions, where we design SHC and BHC unit cells to be stretch-dominated and bending-dominated, respectively. (3) The derived mechanical properties (Figure 7 and **Error! Reference source not found.**) of the unit cells are different. To illustrate, higher compressive strengths are observed for SHC unit cells, while the BHC unit cells absorbs more mechanical energy per unit volume. (4) The amounts of energy absorbed during distinct compressive stages are different for the unit cells. Compared to SHC unit cells, the BHC unit cells absorbs a larger fraction of its mechanical energy during the stress plateau, which is reflected by a more rapid increase of its EAC at plateau stage (Figure S6) for different strain values.

To compare the relative magnitude of the compressive plateau, the strength-normalized average plateau stresses were calculated using Equation (4):

$$\sigma_{NP} = \int_{\varepsilon_\beta}^{\varepsilon_\gamma} \sigma(\varepsilon) d\varepsilon \, / \sigma_\alpha \tag{4}$$

where σ_{NP} is the strength-normalized average plateau stress, σ_α is the peak stress at stage I, ε_β and ε_γ represent the lower and upper strain limits of the plateau stage, respectively. Compared to the unit cells with BHC microstructures that exhibit σ_{NP} = 1.45-1.52, the unit cells with SHC microstructures were observed to possess a lower σ_{NP}, ranging from 0.34 to 0.49. To further analyze the energy absorption behaviors of the hierarchical SHS unit cells, the energy absorption capacity (EAC) [48] was calculated for each strain value based on Equation (5):

$$EAC(\varepsilon_A) = \int_0^{\varepsilon_A} \sigma(\varepsilon) d\varepsilon \, / V_{sphere} \tag{5}$$

where $EAC(\varepsilon_A)$ represents the EAC at strain ε_A and V_{sphere} is the volume of the unit cell. Detailed EAC calculations at different strains suggest that the EAC of the unit cells that possess BHC microstructures exhibited a more significant slope at the plateau stage, while the unit cells with SHC microstructures absorbed more energy at the wavy stage (Figure S6). Overall, the unit cells with SHC microstructures exhibited higher stiffness and strength values, while the BHC-SHS unit cells were ideal energy absorbers to protect more fragile components that cannot suffer high stresses in the wavy stage. The distinctive ranges of the compressive stages and the different quantities of energy absorbed at these stages between the unit cells with different types of the hierarchical microstructures also allowed for designing hierarchical SHS lattices with composite failure mechanisms, which can be achieved by the effective combination of the two topologies within the same SHS lattice structures.

The derived relationships between the microstructural density, relative density, density, compressive strength, modulus, and total EAC of the BHC-SHS and SHC-SHS unit cells are shown in Figure 7, where the derived model parameters are provided in Table S1. Specifically, relative density of the unit cells RD was calculated by dividing structural volume of the unit cell V_{struct} by total volume of the unit cell cubic V_{cubic} as shown in Equation (6):

$$RD = V_{struct}/V_{cubic} \tag{6}$$

In addition, the compressive wavy strength at stages I and II was defined as the maximum compressive stress within the range of those stages. The total EAC was calculated as the energy absorbed per unit volume of the structure until its densification strain as shown in Equation (7):

$$EAC_T = \int_0^{\varepsilon_\gamma} \sigma(\varepsilon) d\varepsilon \, / V_{sphere} \tag{7}$$

where ε_γ is the densification strain and EAC_T is the total EAC. Based on these theoretical calculations and experimental results, the following mechanical models were established:

$$RD\ (\rho_m, T) = A_{RD}(T)\rho_m - B_{RD}(T, \rho_m) \quad (8)$$

$$\rho\ (\rho_m, T) = A_\rho(T)\rho_m + B_\rho(T, \rho_m) \quad (9)$$

$$\sigma_{If}(\rho_m, T) = A_{\sigma_{If}}(T)\rho_m + B_{\sigma_{If}}(T) \quad (10)$$

$$\sigma_{IIf}(\rho_m, T) = A_{\sigma_{IIf}}(T)\rho_m + B_{\sigma_{IIf}}(T) \quad (11)$$

$$EAC(\rho_m, T) = A_{EAC}(T)\rho_m + B_{EAC}(T) \quad (12)$$

where the microstructural density of a unit cell is represented by number of individual topological surfaces ρ_m, T represents the type of the surface topology, RD is the relative density of the unit cell, σ_{If} is the strength of stage I, σ_{IIf} is the strength of stage II, and $EAC(\rho_m, T)$ is the EAC of the unit cell with topology type T and microstructural density ρ_m. The standard deviations of σ_{If}, σ_{IIf}, RD, ρ, and EAC for different measured samples are below 0.2MPa, 0.1 MPa, 0.24%, 3.1 kg/m^3, and 0.2×10^6 J/m^3, respectively. The values of positional parameters A and B are summarized in Table S1, wherein the values of B_{RD}, B_ρ, B_σ, and B_{EAC} are calculated on the basis of the unit systems of % for relative density, kg/m^3 for density, MPa for strength, and J/m^3 for EAC, respectively. Based on these models, a theoretical design guideline was established to facilitate artificial engineering of a preferred distribution of mechanical properties of the unit cells within the design space.

3.2. Multilevel failure mode engineering

Based on the derived mechanical models of the hierarchical SHS unit cells, a multilevel failure mode engineering strategy was proposed. To illustrate this, failure propagation is artificially tailored through the multilevel design of the failure sequences by controlling the microstructural densities of hierarchical SHS unit cells, as shown in Figure 8 (a), where a detailed flow chart in provided in Figure 8 (b). Specifically, the provided design space was first pixelized with size S identical to the cubic dimensions of the hierarchical SHS unit cells, wherein the failure sequence of each pixel was represented by failure factor $F\ (x, y, z)$ ranging from F_1 to F_N. This failure factor was calculated as the safety level that indicated the extent to which each hierarchical SHS unit cell pixel could move prior to its collapse, and the condition in Equation (13) needed to be met to guarantee the correct failure sequence:

$$F_i < F_{i+1}, i = 1, \dots, N-1 \quad (13)$$

Moreover, the stress distribution in the design space was estimated on the basis of the actual load requirements. According to the definition of the failure factor and the estimated stress distribution of the design space, the strengths of stages I and II for the hierarchical SHS unit cell at a certain pixel position (x, y, z) can be derived from Equations (14) to (15):

$$\sigma_{If}(x, y, z) = F(x, y, z)\sigma_e(x, y, z) \quad (14)$$

$$\sigma_{IIf}(x, y, z) = W(x, y, z)\sigma_e(x, y, z) \quad (15)$$

where $F(x, y, z)$ is the pre-designed failure factor, $W(x, y, z)$ represents the safety factor of the secondary wavy stage, and $\sigma_e(x, y, z)$ is the estimated stress located at (x, y, z). Note that the pre-designed failure factor and the safety factor are derived only with respect to the strengths of the hierarchical unit cells (Figure 7 (a)), since these strengths values indicate the stresses of the unit cells at their initial collapses. Other engineerable mechanical properties of the unit cells including the detailed stress-strain curves, stress fields,

modulus, relative density, and density in Figure 7 (b-e) could be used as the potential design information for future researchers to engineer different types of mechanical behaviors for the functional components such as the optimized weight distribution or the pre-engineered stress responses. For adjacent failure levels, Equation (16) should be satisfied to avoid the simultaneous collapse of the wavy stages of their unit cells:

$$W(x_i, y_i, z_i) < F(x_{i+1}, y_{i+1}, z_{i+1}), i = 1, \dots, N-1 \quad (16)$$

where (x_i, y_i, z_i) represents the coordinates of the pixel located at failure level i with failure factor F_i. Combining the results from Equations (10), (11), and (16), the relationship between the wavy strength and microstructural density of the hierarchical SHS unit cells at adjacent failure levels is established in Equations (17) and (18):

$$\sigma_{IIf}(x_i, y_i, z_i)/\sigma_{If}(x_{i+1}, y_{i+1}, z_{i+1}) < C_{i,i+1} \quad (17)$$

$$A_{\sigma_{If}}\big(T(x_i, y_i, z_i)\big)N(x_i, y_i, z_i) - C_{i,i+1}A_{\sigma_{IIf}}\big(T(x_{i+1}, y_{i+1}, z_{i+1})\big)N(x_{i+1}, y_{i+1}, z_{i+1}) < C_{i,i+1}B_{\sigma_{IIf}}\big(T(x_{i+1}, y_{i+1}, z_{i+1})\big) - B_{\sigma_{If}}\big(T(x_i, y_i, z_i)\big) \quad (18)$$

where $C_{A,B} = \sigma_e(x_A, y_A, z_A)/\sigma_e(x_B, y_B, z_B)$ represents the ratio of the estimated stress located in regions A and B. With these conditions satisfied, the structures within the design space would deform and collapse with a pre-engineered failure sequence. To evaluate the components with pre-engineered failure sequences, the load conditions can be applied to evaluate the actual mechanical failure sequences of the designed components. Specifically, either simulational or experimental approach could be made to capture the sequences of the initial collapses of the composing unit cells, where these captured failure sequences will be compared to pre-engineered failure mode for validations. Figure 9(a) shows a case study of applying the hierarchical SHS lattice structures as protective infills for an aerospace turbine blade. In this case study, the failure mode of the turbine blade was artificially engineered to resist the potential impact and protect its shaft from the disintegrated turbine fragments. To illustrate the generality of the proposed method, additional application examples, including a damage-deflective wheel for the space rover and a protective structural infill for a quadradrone, are provided in Figure 9(b-c).

3.3. Biomimetic composite hierarchical SHS lattice structures

Based on the proposed failure mode engineering method, typical failure modes, including "V" shaped, "X" shaped, and layer-wise failure shapes (Figure S7), can be easily developed by the proposed method. According to previous research [3, 49-52], composite structures with layer-wise combinations of mechanical properties are widely found in nature, which provides promoted mechanical properties, such as crack deflection, high energy absorption, and high impact resistance. Furthermore, a layer-wise gradient design of the mechanical properties allowed the structure to exhibit moderate failure and a long stress plateau without undergoing a catastrophic structural collapse while also avoiding a decrease in stress during the compressive process, thereby producing a higher SEA. Therefore, a multilevel laminated failure mode was proposed to develop a composite hierarchical SHS lattice structure with improved SEA, shown in Figure 10. To qualitatively study the effect of the gradient levels for stage I strength $\sigma_{If}(N)$ of hierarchical SHS lattice structures with artificially engineered layer-wise failure mode on their compressive energy absorption behaviors, a maximum and a minimum $\sigma_{If}(N)$ gradients were designed on the basis of the proposed mechanical models of the BHC and SHC hierarchical SHS unit cells. Experimental evaluations of these gradient lattice structures are performed to determine whether a higher gradient value would result

in improved energy absorption, while optimal (either the maximum or minimum) gradient will be applied to the BHC-SHC composite lattice structures on the basis of the obtained results. To further improve the energy absorption performance of the hierarchical SHS lattice structure, a composite hierarchical SHS lattice structure with both BHC and SHC microstructures was developed using a combination of the crystal-inspired hardening mechanism and an optimal strength-gradient. For the detailed composition of the composite hierarchical SHS lattice structure, both SHC and BHC unit cells were layer-wise distributed with an optimal $\sigma_{If}(N)$ gradient, wherein a hardening grain boundary design pattern was included within each layer of the lattice. This composite SHS lattice design was expected to offer a longer plateau with an increased number of failure levels, which were enabled by the distinctive failure mechanisms of different microstructural designs of the hierarchical SHS unit cells. In addition, the artificial grain boundaries could potentially improve the relative magnitude of the stress plateau of the lattice structure by constraining the effect between adjacent grains with different types of the microstructures. The quasi-static compressive tests are used to characterize the mechanical behaviors of these tessellated lattice structures and to evaluate the failure stages of their composing unit cells. The experimentally captured failure sequences and the failure stages of the unit cells are compared with the pre-engineered failure modes for validations. Since the experimental data is adequate to validate the proposed method, the high computational cost simulation of tessellated arrangements is not further conducted to capture the stress field. Upon potential interest of the stress fields, one could use the captured failure stages of the unit cells to compare with the simulation data of single unit cells. Upon potential interest of the stress fields, one could use the captured failure stages of the unit cells to compare with the simulation data of single unit cells.

The compressive results of BHC gradient lattice structures, SHC gradient lattice structures, and BHC-SHC composite lattice structure with optimal gradient levels and artificial grain boundaries are shown in Figure 10. The compressive stress-strain curves and failure propagation diagrams of the printed lattice samples are presented in Figure 11, Figure 12, and Figure 13 (see the evolution of compressive behavior in the AM lattices in Video S3 to Video S7). The quasi-static compressive behaviors and failure mechanisms were first derived for the BHC and SHC lattice structures with two distinct levels of the $\sigma_{If}(N)$ gradients. A composite hierarchical SHS lattice structure was developed through a crystal-inspired hardening distribution strategy of different unit cell microstructures and a biometric laminated failure mode design with an optimal gradient of $\sigma_{If}(N)$, on the basis of the experimental results of the BHC and SHC lattice structures with distinct gradient levels. The compressive test results of the BHC and SHC lattice structures with different gradient levels are summarized in Figure 11 (a) and Figure 12 (a), respectively, wherein gradient level 1 has a larger level of $\sigma_{If}(N)$ gradient than gradient level 2. Similar to the compressive behavior of the hierarchical SHS unit cells, the stress-strain curves of the gradient hierarchical SHS lattice structures with uniform topologies could be characterized into three different stages:

- I: The wavy stage was composed of the first (I_1) and secondary (I_2) sub-wavy stages, wherein a significant fluctuation of stress was observed.
- II: The climbing plateau stage, wherein a steady development of the stress was observed.
- III: The densification stage, wherein the structures of the lattice were forced into contact, and an exponential increase in the stress resulted.

Compared to the SHC gradient lattice structures, a lower stress in the wavy stage and a swifter increment of the plateau stage were observed for BHC gradient lattice structures. Specifically, the values of the strength-normalized average plateau stress (σ_{NP}) for the BHC lattice structures with gradient level 1 and gradient level 2 were 2.1 and 1.3, respectively, while the σ_{NP} values for the SHC lattice structures with gradient level 1 and gradient level 2 were 1.4 and 1.0, respectively. This difference in the relative magnitude of the stress plateau was caused by the distinctive deformation mechanisms of the BHC and SHC cell topologies. As observed in the unit cell mechanical tests, the unit cell with SHC microstructures exhibited higher stiffness and strength values in the wavy stage than that with BHC microstructures owing to its stretch-dominated structural design. For the same topology with different gradient levels, the experimental results indicated that the lattice structure with a larger $\sigma_{If}(N)$ gradient exhibited higher average plateau stress σ_{NP}, delayed densification strain ε_{γ}, and improved SEA, wherefor the specific energy calculated in Equation (19) is defined as the energy absorbed until the densification strain of the lattice structure per unit mass:

$$\text{SEA} = \int_0^{\varepsilon_\gamma} \sigma(\varepsilon) d\varepsilon \, / M_{lattice} \tag{19}$$

where $M_{lattice}$ is the weight of the lattice structure. For instance, the σ_{NP}, ε_{γ}, and SEA for the BHC lattice structure with gradient level 1 are 2.1, 73%, and 13.3 J/g, respectively, which are 55%, 9%, and 35% higher, respectively, than those of the BHC lattice structure with gradient level 2. For the SHC gradient lattice structures, the values of $\sigma_{NP} = 1.4$, $\varepsilon_{\gamma} = 69\%$, and SEA = 13.81 J/g were observed for the gradient level 1, which were 40%, 2%, and 1% higher, respectively, than those for the gradient level 2. To explore the detailed mechanisms that confer the superior energy absorption behavior of hierarchical SHS lattice structures with gradient level 1, the compressive stages of each type of unit cell within the lattice structures at critical strain values are shown in Figure 11b and Figure 12b. The compressive stages of each unit cell were derived according to the experimental failure propagation results and the mechanical modeling of the hierarchical SHS unit cells provided in Figure 6. **Error! Reference source not found.** shows that a reduced overlap of the failure stages between the unit cells with adjacent failure levels was provided by a larger $\sigma_{If}(N)$ gradient in the BHC and SHC gradient lattice structures, wherein a larger portion of the wavy stages of the unit cells contributed to the plateau phase of the resulting lattice structures. This phenomenon led to delayed structural densification and an increased normalized average plateau stress, which resulted in an improved SEA. For instance, the BHC lattice structure with gradient level 2 experienced an overlapped first wavy stage, secondary wavy stage, plateau stage, and plateau-to-densification stage of the unit cells with ρ_m = 212 and ρ_m = 252 in the strain ranges of $\varepsilon = 0.18 - 0.27$, $\varepsilon = 0.25 - 0.36$, $\varepsilon = 0.36 - 0.42$, and $\varepsilon = 0.42 - 0.67$, respectively, while no overlap was observed prior to the densification stage of each type of unit cell for the BHC lattice structure with gradient level 1. For the SHC lattice structure with gradient level 1, two stage overlaps were found for its unit cells: (1) the unit cells with ρ_m = 320 and ρ_m = 420 at $\varepsilon = 0.33 - 0.42$; and (2) the unit cells with ρ_m = 180, ρ_m = 320, and ρ_m = 420 at $\varepsilon = 0.27 - 0.33$. For the unit cells of the SHC lattice structure with gradient level 2, three overlaps were found: (1) the unit cells with ρ_m = 260 and ρ_m = 320 at $\varepsilon = 0.24 - 0.32$; (2) the unit cells with ρ_m = 260 and ρ_m = 320, and ρ_m = 380 at $\varepsilon = 0.32 - 0.42$; and (3) the unit cells with ρ_m = 320 and ρ_m = 380 at $\varepsilon = 0.42 - 0.63$. Based on the experimental capture summarized in Table 5, the actual failure modes of the gradient hierarchical SHS lattice structures are compared with the pre-engineered ones in Figure 11 (c-d) and Figure

12 (c-d). The comparison results validated that the successful achievement of the laminated failure sequence, where the failure surface gradually propagate layer-wise as compression process continues.

Based on the comparison analysis of the hierarchical lattices engineered with the maximum and minimum gradients, the BHC-SHC composite lattice structure was engineered to possess layer-wise composition of the unit cells from the BHC and SHC lattice structures with gradient level 1 (maximum gradient) and artificial grain boundaries, where a detailed design diagram of this is shown in Figure 10. The stage-overlaps of the experimental results are carefully compared between the gradient structures and the BHC-SHC composite lattice structure to validate the constraining effect of its grain boundaries. According to the compressive test results shown in Figure 13(a), a significant improvement in the stress magnitude for the plateau stage and a noticeable delay in the densification strain are obtained. Figure 13(b) visualizes the corresponding compressive stages for different unit cells of the BHC-SHC composite lattice structure during compression, which was further summarized in **Error! Reference source not found.**. The results indicated that an increased number of failure levels was observed for the BHC-SHC composite lattice structure because of the combination of two unit-cell topologies with different failure mechanisms. Moreover, it was observed that the constraining effects between the boundaries of different cell topologies shifted the failure sequence of the unit cells with SHC microstructures earlier such that a greater stress magnitude occurred during the plateau stage of the BHC-SHC composite lattice structure. Quantitively, the BHC-SHC composite lattice entered 10 sub-stages before densification, wherein σ_{NP} =2 and $\varepsilon_\gamma = 0.75$ were obtained.

To further evaluate the mechanical performance of the BHC gradient, SHC gradient and BHC-SHC composite lattice structures, the normalized average plateau stress, densification strain, specific strength, and SEA were provided in Figure 14 and numerically summarized in Table 6, whose specific strength (SS) is calculated using Equation (20):

$$\mathrm{SS} = \frac{\sigma_{1f}}{\rho} \tag{20}$$

where ρ is the density of the lattice structure. It was found that the BHC-SHC composite lattice had an increased SEA value of 15.25 J/g, which was 10.4% higher than that of the SHC-G1 lattice and 14.3% higher than that of the BHC-G1 lattice with a lower specific strength. This was due to the fact that BHC-SHC composite lattice possessed a higher average stress plateau ($\overline{\sigma_{\beta-\gamma}}$ 4.5% and 17% higher than SHC and BHC lattice with maximum gradient level, respectively) with an extended duration (ε_γ 8.7% and 2.7% higher than SHC and BHC lattice with maximum gradient level, respectively) than the BHC and SHC gradient lattice structure at the plateau stage, which accounts for the largest fraction of the total mechanical energy absorbed. The high plateau magnitude of BHC-SHC composite lattice is attributed its pre-engineered artificial grain boundaries, where the constraining effects between the soft BHC grains and stiff SHC grains improves the magnitude of stress during the structural deformation. The extended plateau duration of BHC-SHC composite lattice is caused by its large number of failure stages Table 5, which is in line with the design expectations. Indeed, the BHC-SHC composite lattice structure could preserve a low specific strength while possessing the largest SEA, which made it an ideal energy absorber for components that cannot withstand high stress. Theoretical derivations were performed to further understand this phenomenon. Within the BHC-SHC composite lattice structure, the soft BHC grains were inserted between stiff grains formed by the SHC microstructures, so that the stiffness and resulting strength of the structure

were reduced by the rule-of-mixture and the Reuss model [53]. According to the rule-of-mixture and the deformation stages of the unit cells, the strength of the BHC-SHC composite lattice at $\varepsilon = \varepsilon_2$ can be modeled using Equations (21)-(24):

$$E_{BHC-SHC,1} = \frac{5}{9}E_{BHC,\rho_m=132} + \frac{4}{9}E_{SHC,\rho_m=180} \quad (21)$$

$$E_{BHC-SHC,2} = \frac{4}{9}E_{BHC,\rho_m=212} + \frac{5}{9}E_{SHC,\rho_m=320} \quad (22)$$

$$E_{BHC-SHC,3} = \frac{5}{9}E_{BHC,\rho_m=282} + \frac{4}{9}E_{SHC,\rho_m=420} \quad (23)$$

$$\sigma_{BHC-SHC\alpha} = \frac{3E_{BHC-SHC,1}E_{BHC-SHC,2}E_{BHC-SHC,3}}{E_{BHC-SHC,1}E_{BHC-SHC,2}+E_{BHC-SHC,2}E_{BHC-SHC,3}+E_{BHC-SHC,1}E_{BHC-SHC,3}}\varepsilon_2 \quad (24)$$

where $E_{CHC,F1}$, $E_{CHC,F2}$, and $E_{CHC,F2}$ are the effective moduli of the first, second, and third lattice layers, respectively; $E_{BHC,\rho_m=132}$, $E_{BHC,\rho_m=212}$, $E_{BHC,\rho_m=282}$, $E_{SHC,\rho_m=180}$, $E_{SHC,\rho_m=320}$, and $E_{SHC,\rho_m=420}$ are the moduli of the unit cells with different types and densities of the microstructures calculated by Equation (9); and $\sigma_{BHC-SHC\alpha}$ is the strength of the first wavy stage for the BHC-SHC composite lattice. Based on Equations (18)-(21), the modulus of each BHC-SHC composite lattice layer was found to be decreased by the moduli of the BHC unit cells, whereas it was estimated by the Reuss model that a further reduction in the lattice strength originated from the tandem connection of the lattice layers. To compare the experimental failure mode of BHC-SHC composite lattice with pre-engineered failure mode, the information summarized in Table 5 are used to visualize the propagation of the failure surface in Figure 12c. As expected, the unit cells of BHC-SHC composite lattice generally collapse in a layer-wise manner with fluctuations at the artificial grain boundaries through different layers. This indicates that the triggering of the constraining effect at the artificial grain boundaries, since the SHC unit cells with postponed layer-wise failure with constraint the further deformation of their adjacent BHC unit cells.

For a direct comparison between the results of this work and those of the recent publications related to lightweight structures, including aluminum alloy foams, aluminum alloy lattice structures, and different SHS designs, the corresponding SEA, density-normalized plateau stress, densification strain, and density data are summarized in Ashby charts (Figure 15). In general, the BHC-SHC composite structure exhibited a considerably higher SEA than the summarized lightweight lattice structures fabricated using the aluminum alloy and different SHS designs within the density range of 0-1000 kg/m^3, while being capable of maintaining a low-density value of 215 kg/m^3. Specifically, the results indicated that the BHC-SHC composite structure exhibited significantly improved SEA, higher density-normalized plateau stress, and better deformation capability compared to the recently reported lightweight aluminum alloy structures and various SHS designs. For instance, the BHC-SHC composite structure possessed an SEA of 15.5 J/g and density-normalized plateau stress of 33 MPa$\cdot$ cm^3/g, which was 72% and 50% greater, respectively, than that of the aluminum alloy lattice structures. For the perforated SHS with large deformation before densification, its SEA at ε_γ=0.75 was still 35% lower than that of the BHC-SHC composite lattice structure. The lightweight advantage of BHC-SHC composite structure is attributed by the hollow structure of its unit cell and the proposed bio-inspired surface hierarchical architectures. These features allow the proposed hierarchical SHS lattice structure to exhibit a reduced weight while being mechanically efficient compared to the existing lattice structures and SHSs. The outstanding SEA performances of the BHC-SHC composite structure are mainly contributed by its delayed densification and improved plateau stress. Compared to the reported lattice structures and foams, the BHC-SHC composite structure exhibits a precisely controlled

failure sequence with a large number of failure stages (**Error! Reference source not found.**). This slowly-propagated structural failure effectively delayed the densification of BHC-SHC composite structure. In addition, the BHC-SHC composite structure is designed with a crystal-inspired grain boundary hardening mechanism, which provides the constraining effects between the SHC and BHC unit cells with overlaps of their failure stages (**Error! Reference source not found.**).

4. Conclusions and future work

There is an increasing demand of protective lightweight structures in aerospace industries, which prefers a simultaneous satisfaction of multiple mechanical advances including long stress plateau, high plateau, and large magnitude of plateau-to-strength ratio for the new generation of energy absorption lattice structures. However, conventional design and modelling method usually involves uniform lattice design, or the structural design with simple microstructural variations, which is difficult to satisfy the requirement of mechanical properties in future lightweight structures. In this study, a high-energy-absorption biometric hierarchical composite SHS lattice design is proposed with a pre-engineered layer-wise failure mode and artificial grain boundaries, where the following conclusions are reached:

(1) The conventional SHS lattice structures are redesigned with biometric bending-dominated and stretch-dominated hierarchical honeycomb microstructures to effectively absorb energies with reduced weight.

(2) Systematic studies are conducted to reveal the relationships between the microstructural densities and mechanical properties of BHC and SHC unit cells. The mechanical behaviors of the unit cells within the composite hierarchical lattice structures can be controlled through tailoring the microstructural densities.

(3) A failure mode engineering method is proposed, where the failure sequence of the composite SHS lattice structure is globally controlled through engineering the mechanical properties of its unit cells. Based on this method, a general design paradigm of additively manufactured high-energy-absorption lattice structure is achieved for different protective applications.

(4) A BHC-SHC composite lattice structure with a gradient failure sequences and grain boundary hardening mechanism was developed, where the SEA, densification strain, and the density-normalized plateau magnitude of the proposed lattice structure is 72%, 50%, and 7% higher than the reported energy-absorption material designs with similar densities.

This work inspires four research directions. First, the mechanical effects of surface topologies other than honeycomb can be studied for SHS lattice structures. Second, because the proposed failure mode engineering method is not limited to SHS lattice structures, it can be applied for other types of surface-dominated lattice structures such as the triply periodic minimal surface lattice. Third, more design parameters such as the size, beam thickness, and shell thickness of the hierarchical SHS unit cells could be investigated. Finally, more bio-inspired toughening mechanisms can be studied and achieved on the basis of the microstructural-failure-mode-design method proposed in this paper.

Acknowledgements

This work was sponsored by the National Natural Science Foundation of China (52075327 and 52004160); Shanghai Sailing Program (20YF1419200); Natural Science Foundation of Shanghai (20ZR1427500); and Major Science and Technology Project of Huaibei (Z2020001). H.Z. Wang also acknowledged the support from the Marie Skłodowska-Curie Individual Fellowships (896742). CLAL is grateful for the support from MAPP: EPSRC Future Manufacturing Hub in Manufacture using Advanced Powder Processes (EP/P006566/1), Manufacturing by Design (EP/W003333/1) and Made Smarter Innovation-Materials Made Smarter Research Centre (EP/V061798/1), and Data-driven, Reliable, and Effective

Additive Manufacturing using multi-BEAM technologies (EP/W037483/1)

References

[1] Mueller J, Raney JR, Shea K, Lewis JA. Architected lattices with high stiffness and toughness via multicore-Shell 3D printing. Advanced Materials. 2018;30(12):1705001.
[2] Babaee S, Shim J, Weaver JC, Chen ER, Patel N, Bertoldi K. 3D soft metamaterials with negative Poisson's ratio. Advanced Materials. 2013;25(36):5044-9.
[3] Gao Z, Li D, Dong G, Zhao YF. Crack path-engineered 2D octet-truss lattice with bio-inspired crack deflection. Additive Manufacturing. 2020;36:101539.
[4] Sadeghzade S, Emadi R, Salehi M, Tavangarian F, Ramini A. Crack propagation and toughening mechanisms of bio-inspired artificial spicules fabricated by additive manufacturing technique. Theoretical and Applied Fracture Mechanics. 2020;110:102797.
[5] Pham M-S, Liu C, Todd I, Lertthanasarn J. Damage-tolerant architected materials inspired by crystal microstructure. Nature. 2019;565(7739):305.
[6] Fernandes P, Pinto R, Correia N. Design and optimization of self-deployable damage tolerant composite structures: A review. Composites Part B: Engineering. 2021;221:109029.
[7] Chen Y, Wang L. Bio-inspired heterogeneous composites for broadband vibration mitigation. Scientific reports. 2015;5:17865.
[8] Shan S, Kang SH, Raney JR, Wang P, Fang L, Candido F, et al. Multistable architected materials for trapping elastic strain energy. Advanced Materials. 2015;27(29):4296-301.
[9] Shi J, Mofatteh H, Mirabolghasemi A, Desharnais G, Akbarzadeh A. Programmable multistable perforated shellular. Advanced Materials. 2021;33(42):2102423.
[10] Akbari M, Mirabolghasemi A, Bolhassani M, Akbarzadeh A, Akbarzadeh M. Strut-Based Cellular to Shellular Funicular Materials. Advanced Functional Materials. 2022;32(14):2109725.
[11] Niknam H, Akbarzadeh A. Graded lattice structures: Simultaneous enhancement in stiffness and energy absorption. Materials & Design. 2020;196:109129.
[12] Song J, Zhou W, Wang Y, Fan R, Wang Y, Chen J, et al. Octet-truss cellular materials for improved mechanical properties and specific energy absorption. Materials & Design. 2019;173:107773.
[13] Lyons B. Additive manufacturing in aerospace: Examples and research outlook. The Bridge. 2014;44(3).
[14] Singh R, Lee P, Dashwood R, Lindley T. Titanium foams for biomedical applications: a review. Materials Technology. 2010;25(3-4):127-36.
[15] Nazir A, Abate KM, Kumar A, Jeng J-Y. A state-of-the-art review on types, design, optimization, and additive manufacturing of cellular structures. The International Journal of Advanced Manufacturing Technology. 2019;104(9-12):3489-510.
[16] Zhang J, Lu G, You Z. Large deformation and energy absorption of additively manufactured auxetic materials and structures: A review. Composites Part B: Engineering. 2020;201:108340.
[17] Wang P, Yang F, Lu G, Bian Y, Zhang S, Zheng B, et al. Anisotropic compression behaviors of bio-inspired modified body-centered cubic lattices validated by additive manufacturing. Composites Part B: Engineering. 2022;234:109724.
[18] Zhang J, Yanagimoto J. Topology optimization of CFRP hierarchical pyramidal structures fabricated by additive manufacturing. Composites Part B: Engineering. 2021;224:109241.
[19] Yuan S, Chua CK, Zhou K. 3D-printed mechanical metamaterials with high energy absorption. Advanced Materials Technologies. 2019;4(3):1800419.
[20] Sajadi SM, Vásárhelyi L, Mousavi R, Rahmati AH, Kónya Z, Kukovecz Á, et al. Damage-tolerant 3D-printed ceramics via conformal coating. Science Advances. 2021;7(28):eabc5028.
[21] Gao ZY, Yu TX, Zhao H. Mechanical Behavior of Metallic Hollow Sphere Materials: Experimental Study. Journal of Aerospace Engineering. 2008;21(4):206-16.
[22] Jsab C, Dh B, Sl C, Wl A, Dw C, Qs A, et al. Energy-absorption behavior of metallic hollow sphere structures under impact loading. Engineering Structures.226.
[23] Stylianos Y, Orestes M, Votsis RA, Brennan FP. Compressive Properties of Granular Foams of Adhesively Bonded Steel Hollow Sphere Blocks. Mechanics Research Communications. 2018:S0093641318301587-.
[24] Dai M, Liang J, Cheng C, Wu Z, Lu J, Deng J. Large Deformation and Energy Absorption Behaviour of Perforated Hollow Sphere Structures under Quasi-Static Compression. Materials. 2021;14(13):3716.
[25] Yu TX, Karagiozova D, Gao ZY. The Dependence of the Energy-absorption Capacity of Metal Hollow Sphere Materials on Their Relative Density. Engineering Plasticity and Its Applications from Nanoscale to Macroscale pt1; Key Engineering Materials; vol340-3412007.
[26] Rocklin D, Zhou S, Sun K, Mao X. Transformable topological mechanical metamaterials. Nature communications. 2017;8(1):1-9.

[27] Li MZ, Stephani G, Kang KJ. New Cellular Metals with Enhanced Energy Absorption: Wire-Woven Bulk Kagome (WBK)-Metal Hollow Sphere (MHS) Hybrids. Advanced Engineering Materials. 2011;13(1-2):33-7.
[28] Santa Maria JA, Schultz BF, Ferguson J, Gupta N, Rohatgi PK. Effect of hollow sphere size and size distribution on the quasi-static and high strain rate compressive properties of Al-A380-Al2O3 syntactic foams. Journal of materials science. 2014;49(3):1267-78.
[29] Liu Y, Wu HX, Lu G, Wang B. Dynamic Properties of Density Graded Thin-Walled Metal Hollow Sphere Arrays. Mechanics of Composite Materials & Structures. 2013;20(6):478-88.
[30] Zhang Z, Jones D, Yue S, Lee P, Jones J, Sutcliffe C, et al. Hierarchical tailoring of strut architecture to control permeability of additive manufactured titanium implants. Materials Science and Engineering: C. 2013;33(7):4055-62.
[31] Sercombe TB, Xu X, Challis V, Green R, Yue S, Zhang Z, et al. Failure modes in high strength and stiffness to weight scaffolds produced by Selective Laser Melting. Materials & Design. 2015;67:501-8.
[32] Manno R, Gao W, Benedetti I. Engineering the crack path in lattice cellular materials through bio-inspired micro-structural alterations. Extreme Mechanics Letters. 2019;26:8-17.
[33] Gu GX, Libonati F, Wettermark S, Buehler MJ. Printing nature: Unraveling the role of nacre's mineral bridges. J Mech Behav Biomed Mater. 2017:S1751616117301959.
[34] Gu GX, Takaffoli M, Hsieh AJ, Buehler MJ. Biomimetic additive manufactured polymer composites for improved impact resistance. Extreme Mechanics Letters. 2016:317-23.
[35] Meza LR, Zelhofer AJ, Clarke N, Mateos AJ, Greer JR. Resilient 3D hierarchical architected metamaterials. Proceedings of the National Academy of Sciences of the United States of America. 2015;112(37).
[36] Xiang J, Du J. Energy absorption characteristics of bio-inspired honeycomb structure under axial impact loading. Materials Science and Engineering: A. 2017;696:283-9.
[37] Schultz J, Griese D, Ju J, Shankar P, Summers JD, Thompson L. Design of honeycomb mesostructures for crushing energy absorption. Journal of Mechanical Design. 2012;134(7).
[38] Bates SR, Farrow IR, Trask RS. 3D printed polyurethane honeycombs for repeated tailored energy absorption. Materials & Design. 2016;112:172-83.
[39] Gibson LJ, Ashby MF. Cellular solids: structure and properties: Cambridge university press; 1999.
[40] McNeel R. Rhinoceros 3D, Version 6.0. Robert McNeel. Associates: Seattle, WA, USA. 2010.
[41] Schmidtke K, Palm F, Hawkins A, Emmelmann C. Process and mechanical properties: applicability of a scandium modified Al-alloy for laser additive manufacturing. Physics Procedia. 2011;12:369-74.
[42] Gong H, Rafi K, Starr T, Stucker B. Effect of defects on fatigue tests of as-built Ti-6Al-4V parts fabricated by selective laser melting. Solid freeform fabrication symposium: University of Texas Austin, Texas; 2012. p. 499-506.
[43] Maconachie T, Leary M, Lozanovski B, Zhang X, Qian M, Faruque O, et al. SLM lattice structures: Properties, performance, applications and challenges. Materials & Design. 2019:108137.
[44] Olakanmi EO, Cochrane R, Dalgarno K. A review on selective laser sintering/melting (SLS/SLM) of aluminium alloy powders: Processing, microstructure, and properties. Progress in Materials Science. 2015;74:401-77.
[45] Leung CLA, Marussi S, Atwood RC, Towrie M, Withers PJ, Lee PD. In situ X-ray imaging of defect and molten pool dynamics in laser additive manufacturing. Nature communications. 2018;9(1):1-9.
[46] Sing SL, Yeong WY, Wiria FE, Tay BJEM. Characterization of titanium lattice structures fabricated by selective laser melting using an adapted compressive test method. 2016;56(5):735-48.
[47] Deshpande V, Ashby M, Fleck N. Foam topology: bending versus stretching dominated architectures. Acta materialia. 2001;49(6):1035-40.
[48] Al-Saedi DS, Masood S, Faizan-Ur-Rab M, Alomarah A, Ponnusamy P. Mechanical properties and energy absorption capability of functionally graded F2BCC lattice fabricated by SLM. Materials & Design. 2018;144:32-44.
[49] Ying L, Wu HX, Wang B. Gradient design of metal hollow sphere (MHS) foams with density gradients. Composites Part B. 2012;43(3):1346-52.
[50] Mao A, Zhao N, Liang Y, Bai H. Mechanically Efficient Cellular Materials Inspired by Cuttlebone. Advanced Materials. 2021;33(15):2007348.
[51] Koester KJ, Ager J, Ritchie R. The true toughness of human cortical bone measured with realistically short cracks. Nature materials. 2008;7(8):672-7.
[52] Jernkvist LO. On the fracture behaviour of softwood: a combined experimental and computational study of the interaction between fracture behaviour and material anatomy: Luleå tekniska universitet; 2000.
[53] Askeland DR, Phulé PP, Wright WJ, Bhattacharya D. The science and engineering of materials. 2003.

[54] Idris M, Vodenitcharova T, Hoffman M. Mechanical behaviour and energy absorption of closed-cell aluminium foam panels in uniaxial compression. Materials Science and Engineering: A. 2009;517(1-2):37-45.
[55] Jung A, Natter H, Diebels S, Lach E, Hempelmann R. Nanonickel coated aluminum foam for enhanced impact energy absorption. Advanced Engineering Materials. 2011;13(1-2):23-8.
[56] Maskery I, Aboulkhair N, Aremu A, Tuck C, Ashcroft I, Wildman RD, et al. A mechanical property evaluation of graded density Al-Si10-Mg lattice structures manufactured by selective laser melting. Materials Science and Engineering: A. 2016;670:264-74.
[57] Aldoshan A, Khanna S. Effect of relative density on the dynamic compressive behavior of carbon nanotube reinforced aluminum foam. Materials Science and Engineering: A. 2017;689:17-24.

Figures and tables

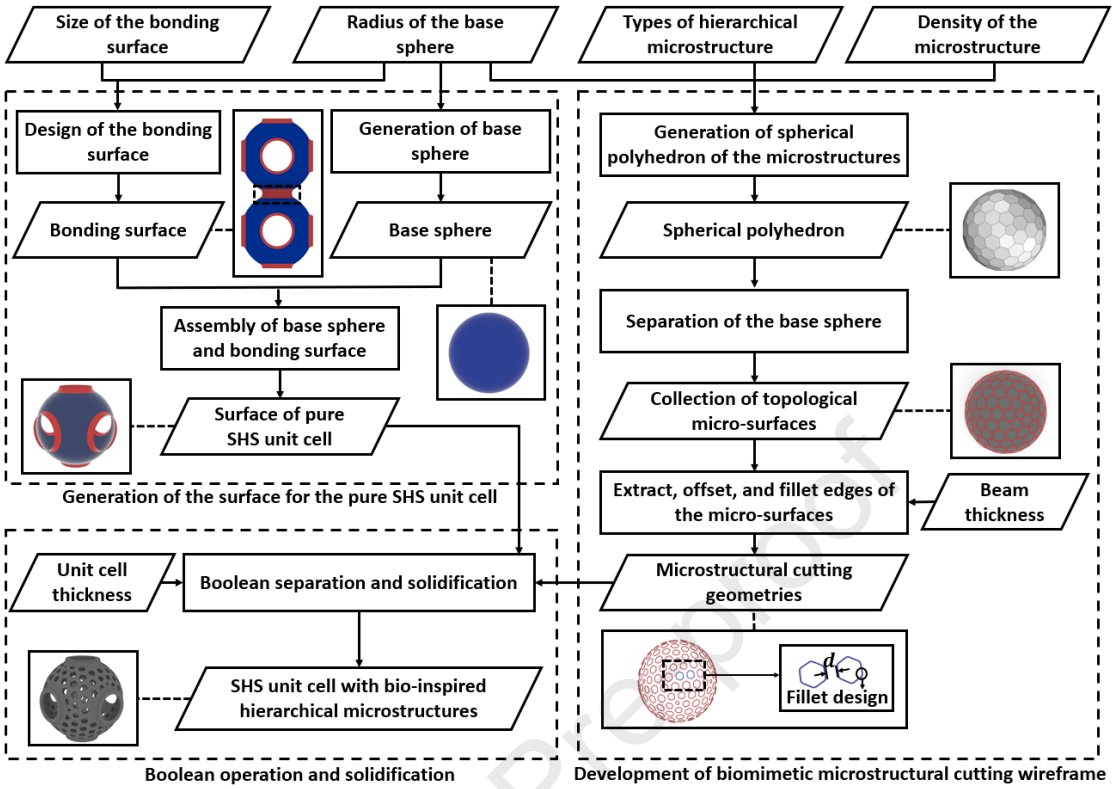

Figure 1. General workflow of SHS unit cells with hierarchical microstructures.

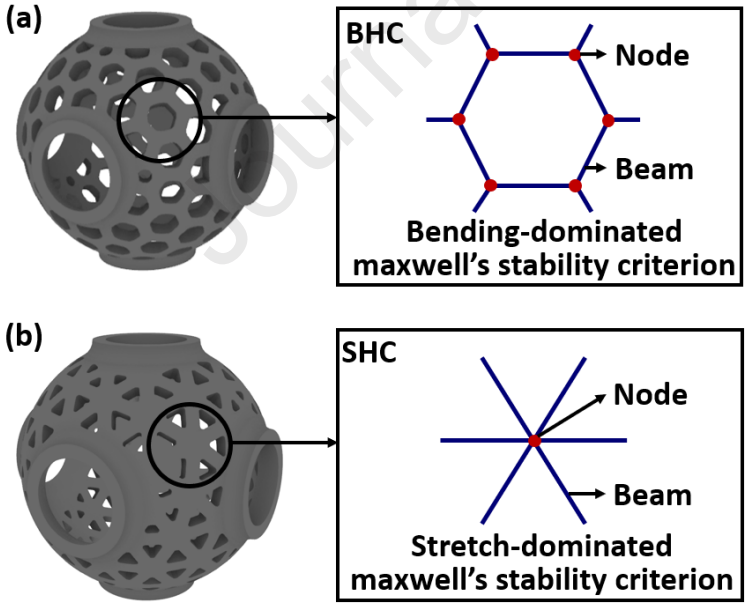

Figure 2. Different microstructural designs of hierarchical SHS unit cells: (a) bending-dominated honeycomb (BHC); and (b) stretch-dominated honeycomb (SHC).

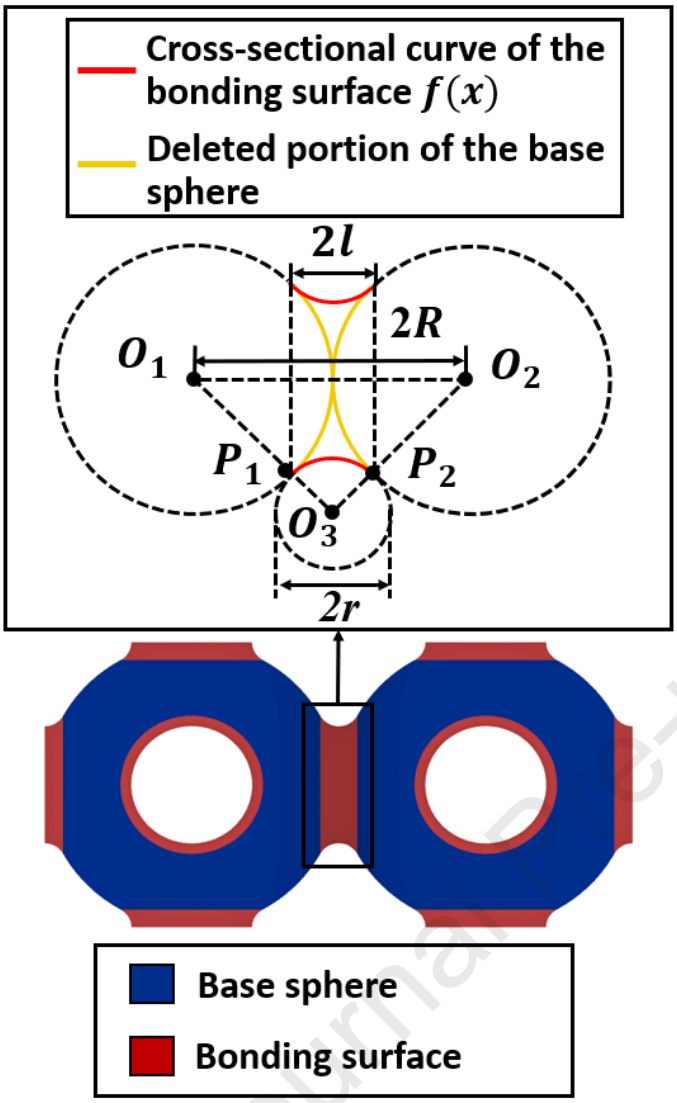

Figure 3. Design of the bonding surface between SHS unit cells.

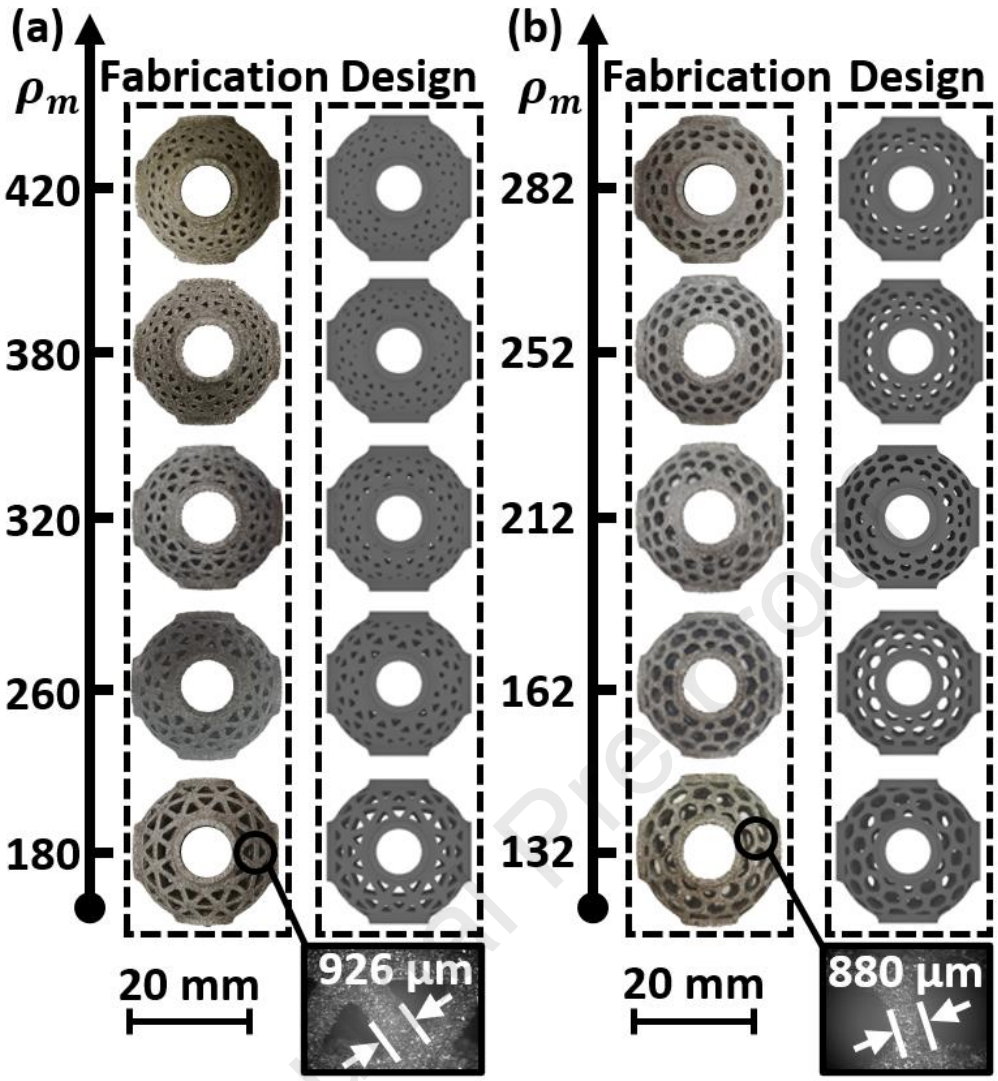

Figure 4. The designed and fabricated hierarchical SHS unit cells with different microstructural densities and representative SEM images of their local surfaces: (a) SHC SHS unit cells; and (b) BHC SHS unit cells. Refer to Figure S2 to Figure S4 for detailed statistical results and of the beam sizes and the fabrication qualities of the printed samples.

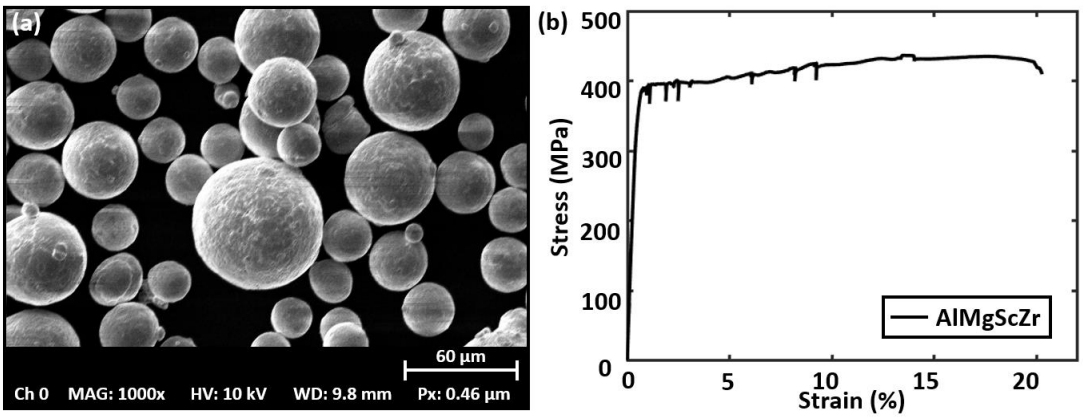

Figure 5. The powder image and the mechanical properties of the building material: (a) SEM image of AlMgScZr powder; (b) experimental stress-strain curve for the SLM AlMgScZr alloy.

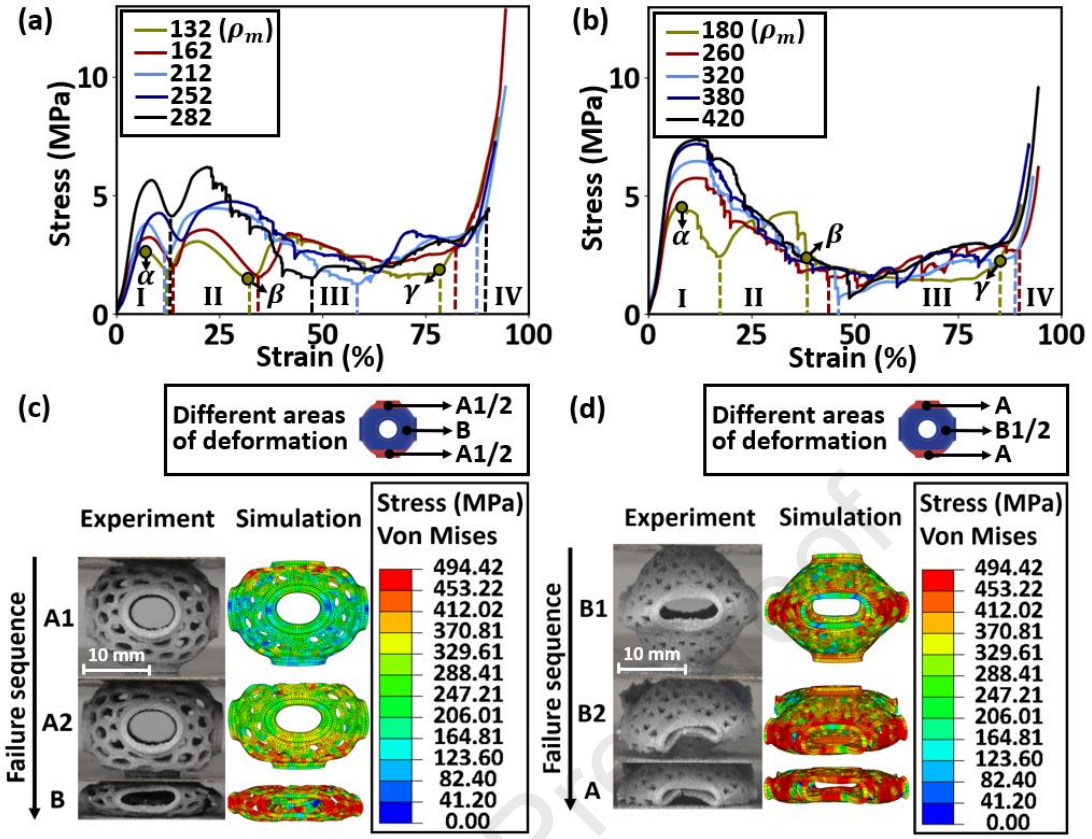

Figure 6. Compressive stress-strain curves and failure mechanisms of hierarchical SHS unit cells: (a) experimental stress-strain curve for SHS unit cells with BHC microstructures; (b) experimental stress-strain curve for SHS unit cells with SHC microstructures; (c) experimental (left) and simulational (right) failure sequence of SHS unit cells with BHC microstructures; and (d) experimental (left) and simulational (right) failure sequence of SHS unit cells with SHC microstructures. I-IV are different failure stages, α represents the initiation of the plastic deformation, β is the beginning of the plateau stage, γ is the densification point, A1/2 are the unit cell edges, and B1/2 are the middle areas of the unit cell.

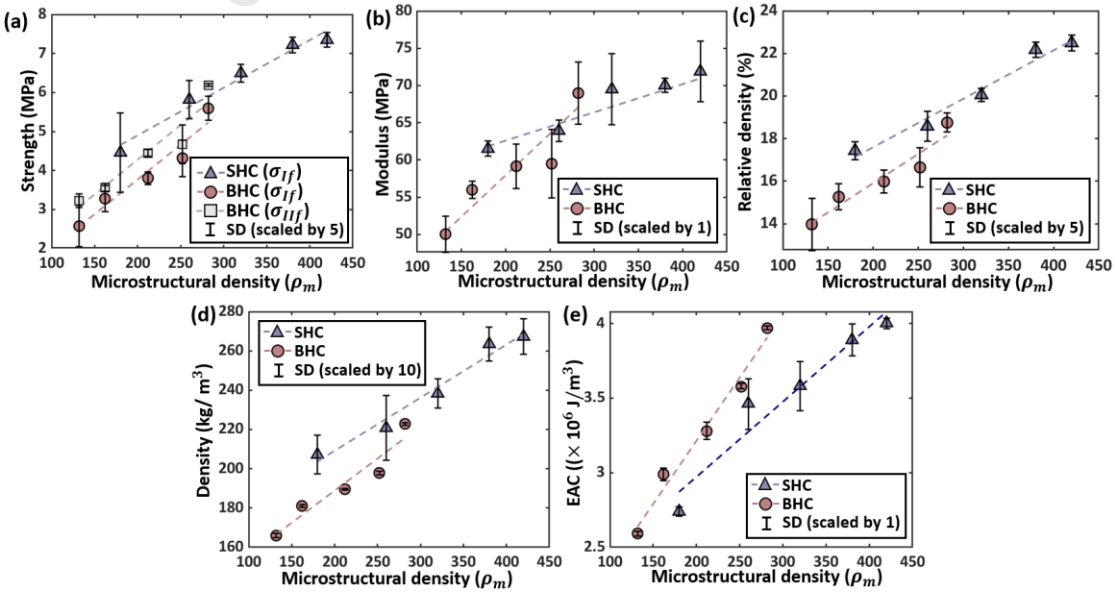

Figure 7. Mechanical modeling of hierarchical SHS unit cells with BHC and SHC microstructures based on experimental results: (a) relationship between the compressive strength and microstructural densities,

where σ_{If} and σ_{IIf} represent the strength for the first wavy stage and secondary wavy stage, respectively; (b) relationship between the compressive modulus and microstructural densities; (c) relationship between the relative density and microstructural densities; (d) relationship between the density and microstructural densities; and (e) relationship between the energy absorption capacity (EAC) at densification strain and microstructural densities.

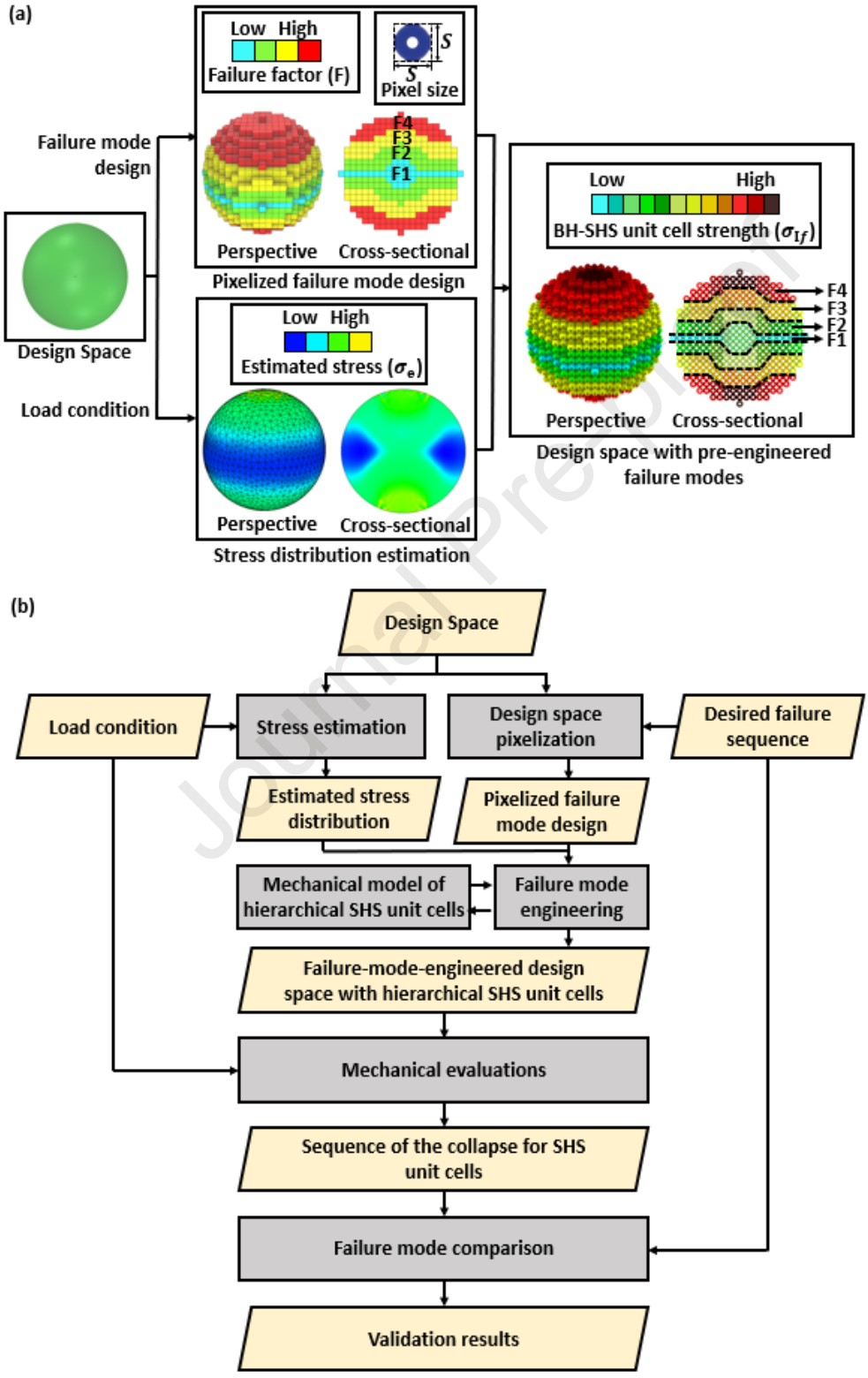

Figure 8. The failure mode engineering method: (a) the design schematics; (b) the detailed flow chart.

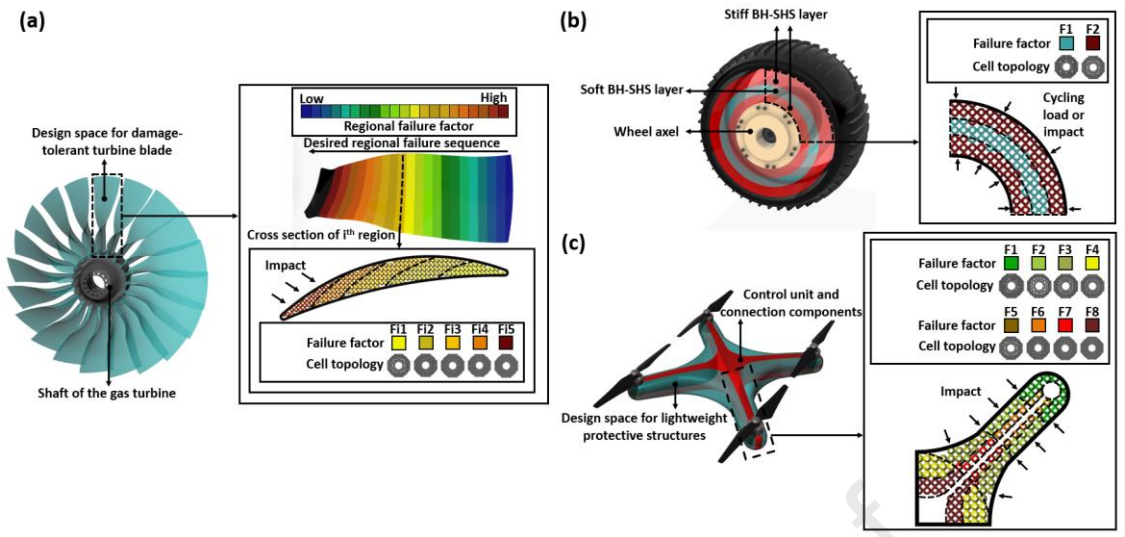

Figure 9. Potential applications of failure-mode-engineered hierarchical SHS lattice structures: (a) a lightweight damage-tolerant turbine blade design with composite hierarchical SHS lattice infills; (b) a space rover wheel with protective damage deflection design using hierarchical SHS infills; and (c) a quadradrone with impact-resistant hierarchical SHS infills.

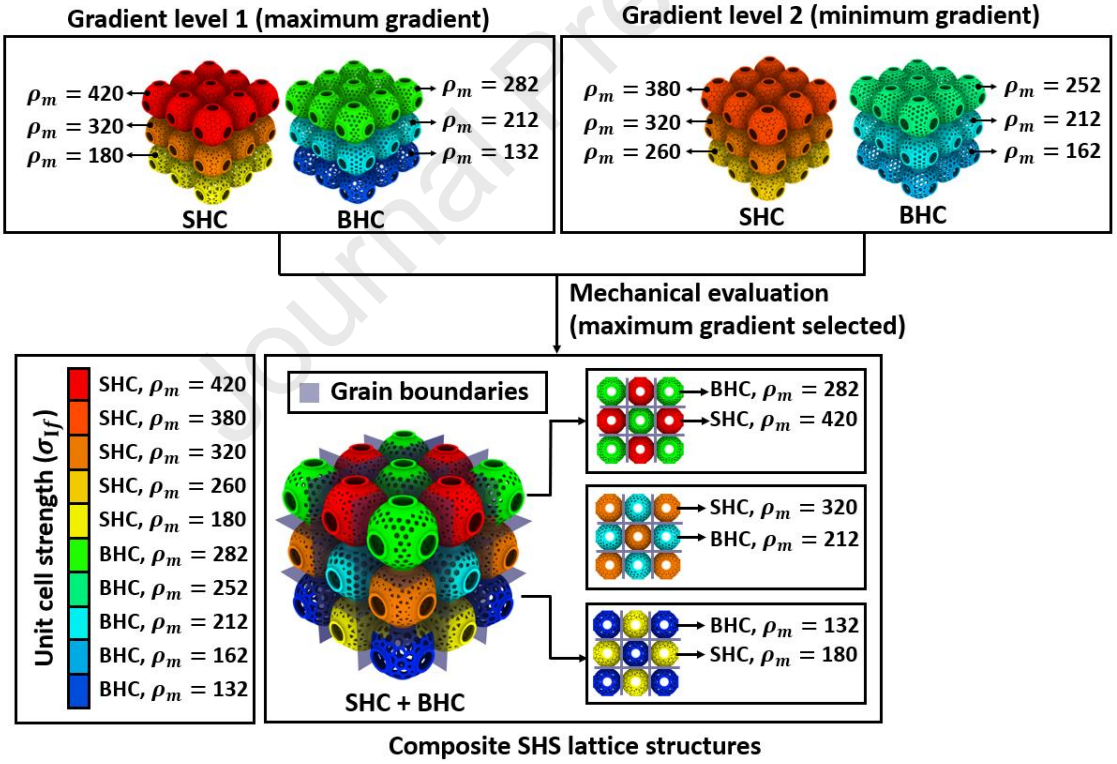

Figure 10. Design of High-energy-absorption hierarchical SHS lattice with optimal gradient level and artificial grain boundaries.

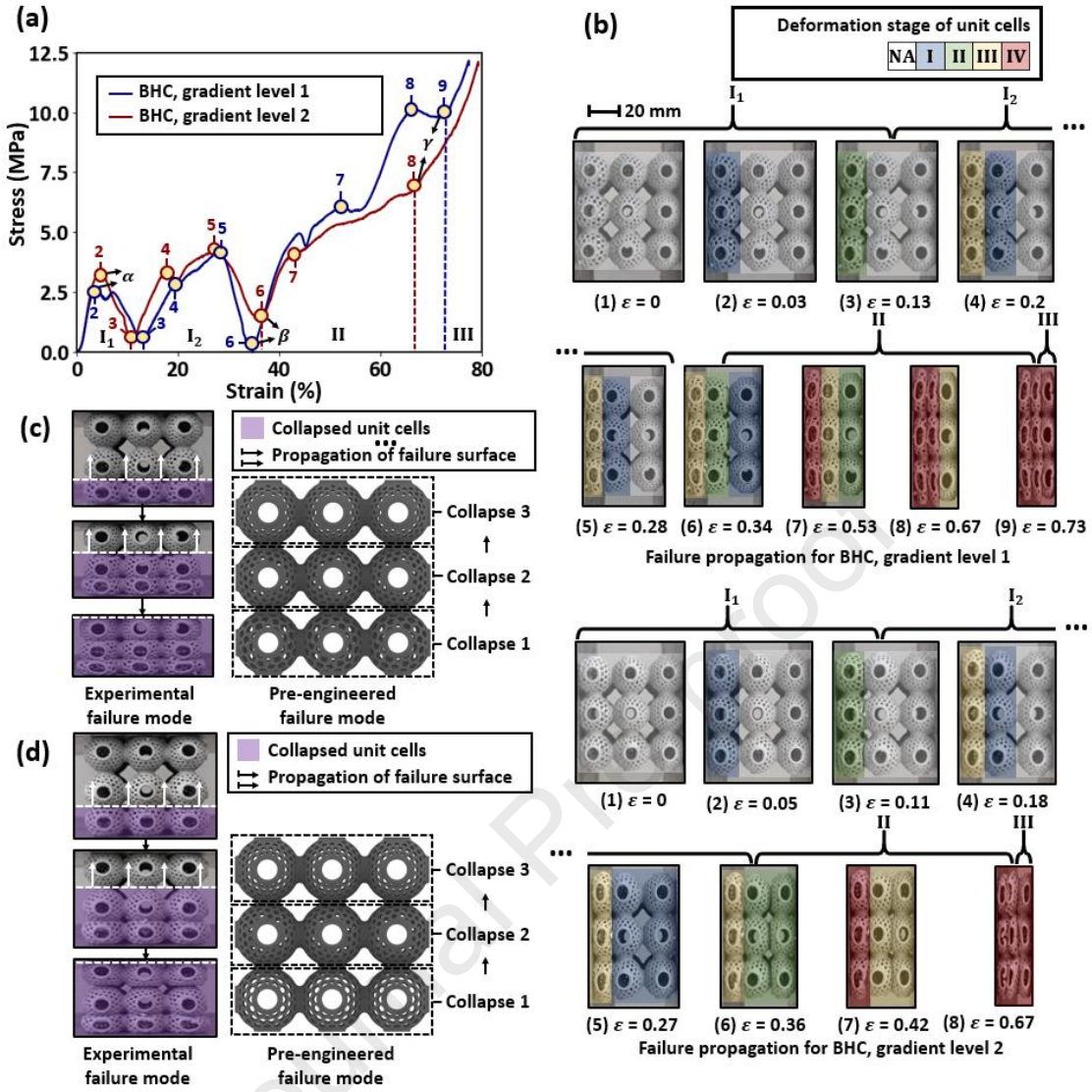

Figure 11 (original Figure 11 (a, c)). The (a) experimental compressive stress-strain curves, (b) failure propagations, (c) failure mode comparison (gradient level 1), and (d) failure mode comparison (gradient level 2) of BHC hierarchical SHS lattice structures with different gradient levels. Note that 1-9 separates different compressive substages of BHC gradient lattice structures, which are summarized in Table 5. α, β, γ are the initiation points of the plastic deformation, plateau stage, and densification stage, respectively.

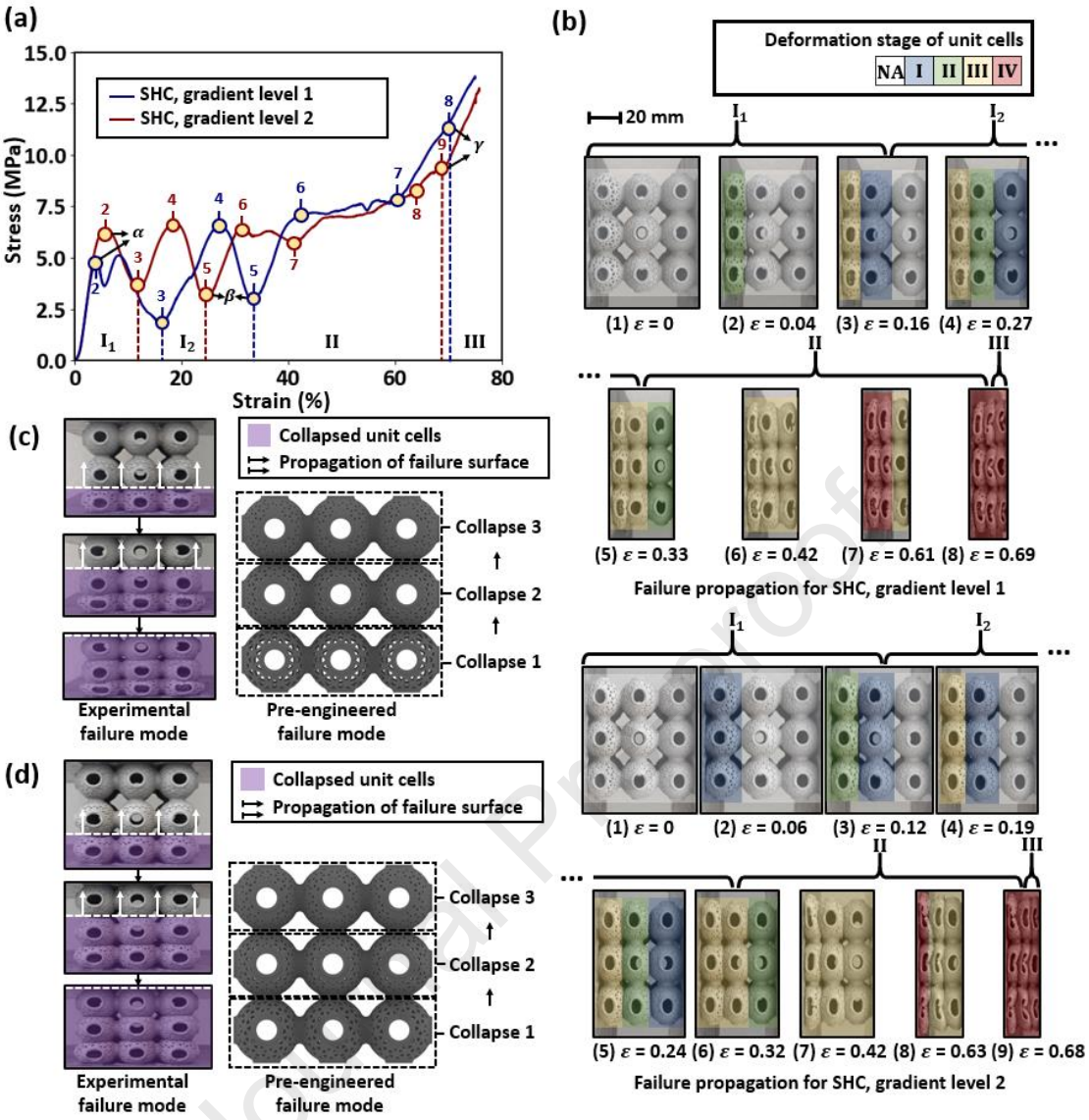

Figure 12 (original Figure 11 (b, d)). The (a) experimental compressive stress-strain curves, (b) failure propagations, (c) failure mode comparison (gradient level 1), and (d) failure mode comparison (gradient level 2) of SHC hierarchical SHS lattice structures with different gradient levels. Note that 1-9 separates different compressive substages of SHC gradient lattice structures, which are summarized in Table 5. α, β, γ are the initiation points of the plastic deformation, plateau stage, and densification stage, respectively.

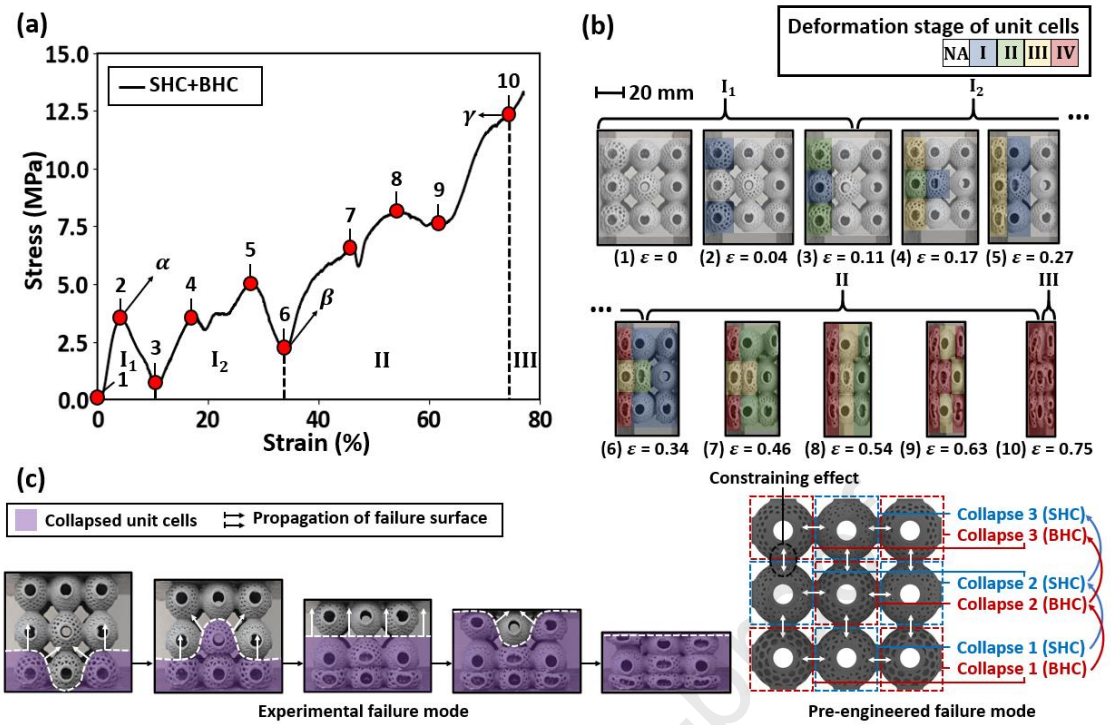

Figure 13 (original Figure 12). The (a) experimental compressive stress-strain curve, (b) failure propagation, and (c) failure mode comparison for the BHC-SHC composite lattice structure with optimal gradient level and artificial grain boundaries. Note that 1-10 separates different compressive substages of BHC-SHC lattice structures summarized in Table 5. α, β, γ are the initiation points of the plastic deformation, plateau stage, and densification stage, respectively.

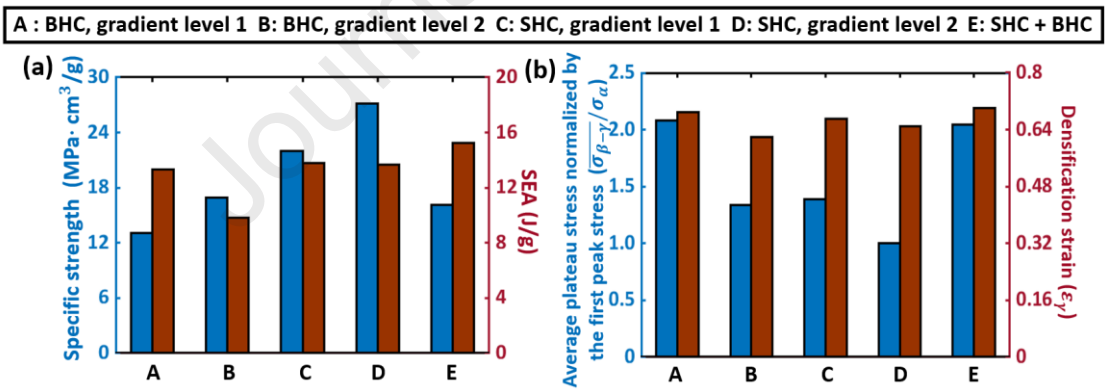

Figure 14. Material property comparison between different hierarchical SHS lattice structures: (a) the experimental specific strength and SEA (SEA); and (b) the experimental strength-normalized plateau magnitude and densification strain.

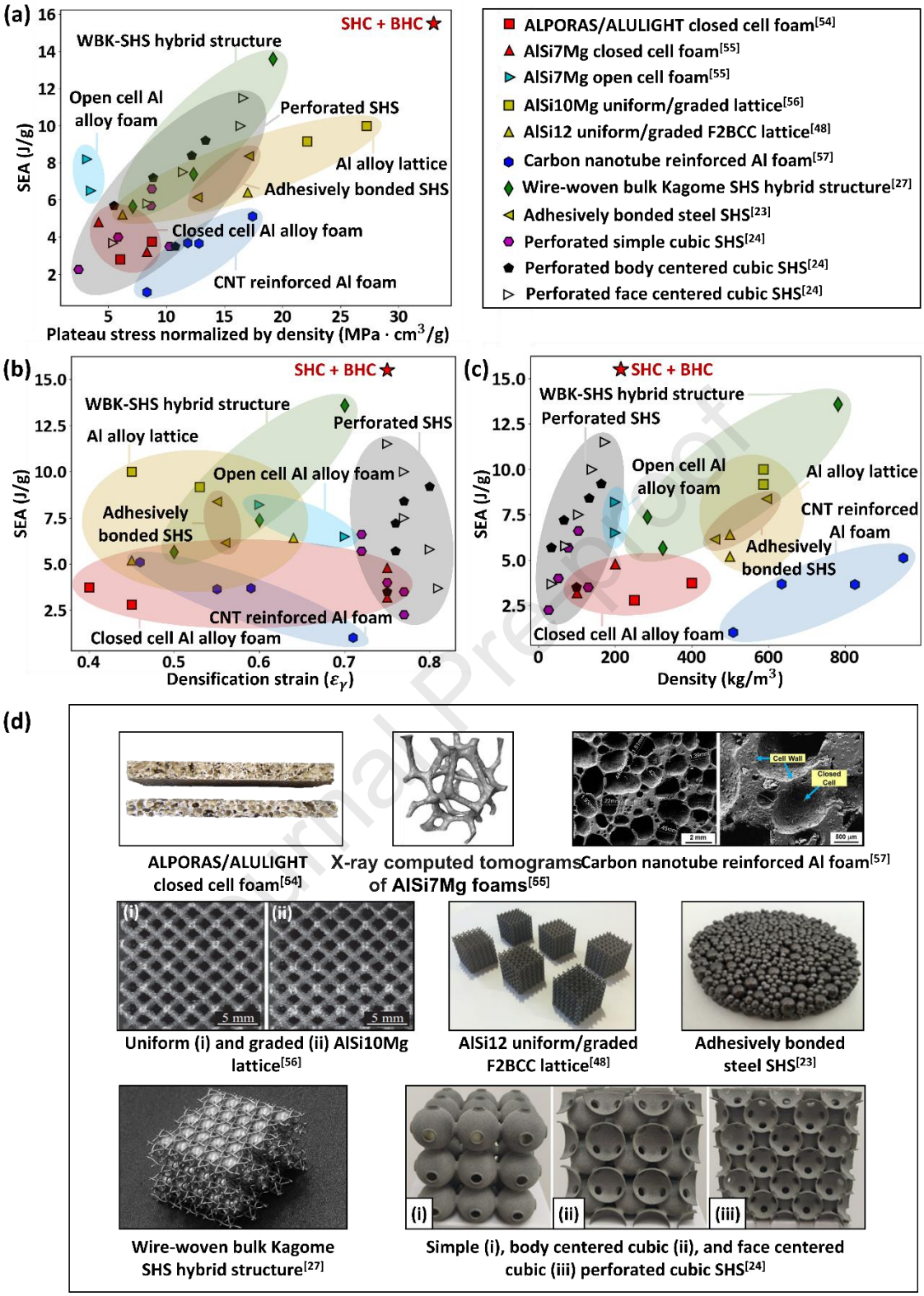

Figure 15 (original Figure 14). Ashby charts reflecting the SEA (SEA) with (a) density-normalized plateau stress, (b) densification strain, and (c) density of lightweight structures including aluminum alloy foams and lattice structures [48, 54-57], different designs of SHS [23, 24, 27], and the BHC-SHC composite SHS lattice structures in this work, where the representative images of the reported lightweight structures are provided in (d).

Table 1. Summary of the design parameter values for the hierarchical SHS unit cells.

Design parameter	Selected range
Beam thickness [mm]	1
Shell thickness [mm]	1
Microstructural density for SHS unit cells with BHC microstructures	132 ~ 282
Microstructural density for SHS unit cells with SHC microstructures	180 ~ 420

Table 2. Building setup and process parameters of the SLM procedure.

Building setup	EOS M280 SLM printer
Layer thickness [μm]	30
Hatch distance [μm]	80
Laser speed [mm/s]	1600
Laser power [W]	370
Beam offset [μm]	20
Stripe width [mm]	5
Overlap [μm]	50

Table 3. Summary of the powder preparation, composition, and drying condition.

Preparation of powder	Elemental mixed
Powder composition	93.6% Al, 4.7% Mg, 0.79% Sc, 0.32% Zr, 0.59% Mn
Dehydration condition prior to printing	75 ℃, 12 hours

Table 4. Comparisons of the mechanical behaviors between BHC and SHC unit cells.

Unit cell topology	Failure mode	Strength (MPa)	Strength-normalized average plateau stresses (MPa / MPa)	Plateau duration (%)
BHC	A1-A2-B	2.57-5.59	1.45-1.52	~70%
SHC	B1-B2-A	4.46-7.35	0.34-0.49	~35%

Table 5. Compressive stages of the unit cells for BHC gradient, SHC gradient, and SHC + BHC lattice structures.

	Compressive stage analysis for gradient level 1					Compressive stage analysis for gradient level 2				
	Lattice structure		ρ_m of the unit cell			Lattice structure		ρ_m of the unit cell		
	Total	Substage	132	212	282	Total	Substage	162	212	252
BHC gradient lattice	I_1	1-2	I	-	-	I_1	1-2	I	-	-
		2-3	II	-	-		2-3	II	-	-
	I_2	3-5	III	I	-	I_2	3-4	III	I	-
		5-6	III	II	I		4-5	III	I	I
	II	6-7	IV	III	II		5-6	III	II	II

		7-8	IV	IV	III	II	6-7	IV	III	III
		8-9	IV	IV	III-IV		7-8	IV	III-IV	III-IV
	III	9-	IV	IV	IV	III	8-	IV	IV	IV
SHC gradient lattice	Lattice structure		ρ_m of the unit cell			Lattice structure		ρ_m of the unit cell		
	Total	Substage	180	320	420	Total	Substage	260	320	380
	I_1	1-2	I-II	-	-	I_1	1-2	I	-	-
		2-3	III	I	-		2-3	II	I	-
	I_2	3-4	III	II	I	I_2	3-4	III	I	-
		4-5	III	III	II		4-5	III	II	I
	II	5-6	III	III	III		5-6	III	III	II
		6-7	IV	IV	III	II	6-7	III	III	III
		7-8	IV	IV	III-IV		7-8	IV	III	III
	III	8-	IV	IV	IV		8-9	IV	IV	III-IV
						III	9-	IV	IV	IV
SHC + BHC lattice	Compressive stage analysis for optimal gradient level									
	Lattice structure		ρ_m of the BHC unit cell			Lattice structure		ρ_m of the SHC unit cell		
	Total	Substage	132	212	282	Total	Substage	180	320	420
	I_1	1-2	I	-	-	-	1-2	-	-	-
		2-3	II	-	-	I	2-3	I	-	-
	I_2	3-4	III	I	-	II	3-4	II	-	-
		4-5	III	I	-	III	4-5	III	I	-
		5-6	IV	II	I	III	5-6	III	II	-
	II	6-7	IV	III	II	III	6-7	III	II	I
		7-8	IV	III	III	IV	7-8	IV	III	II
		8-9	IV	IV	IV	IV	8-9	IV	III-IV	III
		9-10	IV	IV	IV	IV	9-10	IV	IV	III-IV
	III	10-	IV	IV	IV	IV	10-	IV	IV	IV

Table 6. Values of key mechanical indexes for BHC gradient, SHC gradient, and SHC + BHC lattice structures.

Lattice type	Specific strength (MPa·cm^3/g)	SEA (J/g)	Average plateau stress normalized by the first peak stress (MPa/MPa)	Densification strain (%)
BHC lattice with gradient level 1	13.10	13.34	2.08	73
BHC lattice with gradient level 2	16.90	9.85	1.34	67
SHC lattice with gradient level 1	22.02	13.81	1.39	69
SHC lattice with gradient level 2	27.20	13.66	1.00	68
SHC + BHC lattice	16.10	15.25	2.05	75

Highlights

- Spherical hollow lattice structures are first engineered and successfully additively manufactured with honeycomb-inspired hierarchical microstructures.
- Hierarchical lattice unit cells with engineerable mechanical behaviors are developed based on theoretical studies relating their microstructural densities and mechanical performances.
- A failure mode engineering method is proposed through controlling the distribution of hierarchical lattice unit cells with different microstructural densities.
- Ultrahigh specific energy absorption is achieved through a novel lightweight hierarchical lattice structure designed with layer-wise failure mode and artificial grain boundaries.

Declaration of interests

☒ The authors declare that they have no known competing financial interests or personal relationships that could have appeared to influence the work reported in this paper.

☐ The authors declare the following financial interests/personal relationships which may be considered as potential competing interests: